Monthly Notices of the ROYAL ASTRONOMICAL SOCIETY

MNRAS **535,** 3088–3107 (2024) https://doi.org/10.1093/mnras/stae2483
Advance Access publication 2024 November 4

Unveiling gas kinematics and stellar populations in H II regions inside the low-metallicity dwarf nearby galaxy SDSSJ0859 + 3923 with MEGARA at the GTC

M. L. García-Vargas [1]★ E. Carrasco [2] M. Mollá [3] A. Gil de Paz [4,5] J. Gallego,[4,5] J. Iglesias-Páramo,[6] N. Cardiel [4,5] A. Castillo-Morales,[4,5] S. Pascual,[4,5] P. Gómez-Alvarez[1] and A. Pérez-Calpena[1]

[1]*FRACTAL S.L.N.E. Calle Tulipán 2, portal 13, 1A, E-28231 Las Rozas de Madrid, Spain*
[2]*Instituto Nacional de Astrofísica, Óptica y Electrónica (INAOE), Calle Luis Enrique Erro 1, C.P. 72840 Santa María Tonantzintla, Puebla, México*
[3]*Dpto. de Investigación Básica, CIEMAT, Avda. Complutense 40, E-28040 Madrid, Spain*
[4]*Dpto. de Física de la Tierra y Astrofísica, Fac. CC. Físicas, Universidad Complutense de Madrid, Plaza de las Ciencias 1, E-28040 Madrid, Spain*
[5]*Instituto de Física de Partículas y del Cosmos, IPARCOS, Fac. CC. Físicas, Universidad Complutense de Madrid, Plaza de las Ciencias 1, E-28040 Madrid, Spain*
[6]*Instituto de Astrofísica de Andalucía, IAA-CSIC, Glorieta de la Astronomía s/n, E-18008 Granada, Spain*

Accepted 2024 October 30. Received 2024 October 26; in original form 2023 November 25

ABSTRACT

In this study, we present Integral Field Unit observations of the galaxy SDSSJ0859 + 3923, utilizing the MEGARA (Multi Espectrógrafo en GTC de Alta Resolución para Astronomía) instrument on the GTC (Gran Telescopio Canarias) 10.4m telescope. These observations were conducted in two distinct spectral ranges: 4332–5222 Å and 6097–7345 Å, with a high resolving power ($R_{\rm FWHM}\sim$ 6 000), and spatial resolution of 25 pc, considering the galaxy's distance of 8.5 Mpc. Our observations have identified five H II regions, whose precise positions were determined using data from the *Wide Field Camera 3* (ultraviolet and visible) of the *Hubble Space Telescope*, WFC3-UVIS/*HST,* archive images, where we also detected the associated blue underlying continuum linked to the ionized knots. A detailed kinematic analysis of these regions revealed low-velocity dispersion values (around 10 km s^{-1}) in four H II regions, indicating a lack of significant turbulent events. In the fifth region, we observed a peak in velocity dispersion reaching 40 km s^{-1}, which we interpret as the result of hot star winds and/or a recent type-II supernova explosion. We have conducted a comprehensive spectral analysis of the H II regions, obtaining emission-line fluxes that enabled us to confirm the oxygen abundance (12 + log(O/H) = 7.41 ± 0.15) and, using POPSTAR models, to constrain the age and mass of the ionizing young clusters.

Key words: galaxies: individual: SDSSJ0859+3923 – H II regions – galaxies: dwarf – galaxies: abundances – galaxies: star formation.

1 INTRODUCTION

The study of the properties of the eXtremely metal-deficient galaxies (hereafter XMDg) has been an intense research topic for the last years. On the one hand, these works have pursued the understanding of the physical and chemical mechanisms capable to keep the abundance at such low levels. On the other hand, the final objective is to explain what might have happened in the early universe, with a metal content similar to the one measured in XMDg. We devote this section to discuss the numerous samples effects that might be biasing our understanding of these galaxies.

A galaxy is catalogued to be a XMDg if its oxygen abundance, log(O/H), is lower than a given number, whose value has been changing in recent years, from an early value of 12 + log(O/H) ≤ 7.65 (Kunth & Östlin 2000) to the more recent lower limit of 12 + log(O/H) ≤ 7.15 (Hirschauer et al. 2016, hereafter H16). A detailed discussion is given by Carrasco et al. (2022, hereafter C22).

What we call *first bias* is due to the search of XMDg among intrinsically low-luminosity systems. Assuming that these galaxies follow the luminosity (L)–metallicity (Z) relationship, which predicts an intrinsic very low luminosity for the lowest metal-content galaxies (Skillman, Kennicutt & Hodge 1989), XMDg would be less detectable for a given luminosity limit. In fact, the number of observed XMDg has increased with the development of powerful instruments at the largest aperture (≥6.5 m) telescopes.

The other biases are connected to the detection strategy itself. For the last 15 yr, because of the intrinsic low luminosity of XMDg, their search has focused in subsamples showing evidence of star formation. These bursts boost the XMDg luminosity after ionizing the gas, producing a strong and detectable emission-line spectrum (Izotov & Thuan 2007; Izotov, Thuan & Guseva 2012; Guseva et al. 2017; Hirschauer et al. 2018; Izotov et al. 2018, 2019, hereafter I19). This approach has promoted the search of XMDg candidates among

★ E-mail: marisa.garcia@fractal-es.com

the brightest knots in visible emission-line images or low-resolution spectra in surveys, such as the Sloan Digital Sky Survey (SDSS; Abazajian et al. 2005), from which numerous XMDg candidates have been proposed based on emission-line ratios diagnostic diagrams. In particular, the [O III]/Hβ emission-line ratio has been extensively used as a tracer of the age and metallicity of very young star clusters, as predicted by a combination of evolutionary synthesis and photoionization models, under certain hypotheses of the star formation and the gas. Pioneer models for H II regions by García-Vargas, Bressan & Díaz (1995a, b) showed that clusters younger than 5.5 Myr have a relatively hard spectrum able to produce high values of [O III] at moderate and low metallicity. This was later confirmed and improved by Martín-Manjón et al. (2010, hereafter M10), using POPSTAR models by Mollá, García-Vargas & Bressan 2009, hereafter M09) and García-Vargas, Mollá & Martín-Manjón (2013), and CLOUDY (Ferland et al. 1998) code. This observational strategy produces a double-biased samples of XMDg candidates. On the one hand, only galaxies experimenting young star formation episodes are selected, missing the very low-metallicity galaxies with quiet intermediate and old stellar populations (what we call the *second bias*). On the other hand, the lowest luminosity and lowest metallicity XMDg might have also very low mass and, theoretically, less amount of gas to fuel the episodes of star formation, what would make these galaxies be underdetected or just missed in the XMDg candidates samples (*third bias*). The detection of the XMDg out of star-forming episodes and the low-luminosity and super-low-metallicity XMDg might be the main challenge of this research field in the years to come.

Once detected the XMDg candidates during star-forming episodes, from their high [O III]4959, 5007/ Hβ, pointing the low abundance regime, the next step is the confirmation of this very low metallicity from the emission lines and the theoretical prediction of the gas properties (Osterbrock & Ferland 2006; Pérez-Montero 2014). The average electron density, n_e, is determined from density-sensitive gas emission lines like [S II] or [O II] and then, the electron temperature, T_e, of the ionized nebula is assumed to follow T_e ([O III]), which is obtained from the ratio $R_{O3} = I_{(4959} + I_{5007)} / I_{4363}$. This leads to the *fourth bias* in XMDg samples, constraining their metallicity range to that in which a direct oxygen abundance determination is possible, missing those XMDg whose oxygen content was low enough to not produce the [O III] λ 4363 Å line. Moreover, this line is intrinsically very weak, of the order of 1–2 per cent of the intensity of [O III] λ 5007 Å and its measurement is challenging, demanding large-aperture telescopes and long exposure times, what yields an additional bias in the low-metallicity value determination and, very important, its associated error. When no detection of [O III] λ 4363 line is available, the oxygen abundance could be inferred through the 'strong-line methods', based on combinations of strong emission-line intensities of various elements plus theoretical calibrations between these lines and the weakest ones (I19; Pagel et al. 1979). Sometimes these methods give very good results (and discussion here Thuan, Guseva & Izotov 2022) but might also lead to important discrepancies on the lowest metallicity regime (and references therein Andrews & Martini 2013). The publication of the Arecibo Legacy Fast ALFA blind [H I] survey, ALFALFA (Giovanelli et al. 2005; Haynes et al. 2011, 2018; Giovanelli et al. 2013), opened a new technique for identifying XMDg candidates based on selecting galaxies with low H I mass from ALFALFA data and bright optical emission-line counterpart in the SDSS. The result was SHIELD, survey of H I in extremely low-mass dwarfs (Cannon et al. 2011), which produced the discoveries of few more XMDg, as Leoncino (H16; C22). However, the categorization as XMDg with this technique relied again entirely on measuring the oxygen abundance using [O III] lines detected in the visible spectrum.

We ought to mention another issue connected to the problem of dating the hidden stellar populations in XMDg, which is usually missed in the discussions. This is the fact that the detection of the ionized gas emission lines is possible only once the nebula has reached the equilibrium state, and then is when we observe the spectrum of the gas ionized by a cluster that has evolved along the nebula equilibrium time, t_{eq}. M10 computed t_{eq} for nebulae ionized by young ionizing clusters in a range of age and metallicity. They concluded that, for a given value of the metallicity, neither the total number of ionizing photons (mostly connected to the cluster mass) nor the ionizing spectrum shape (depending on cluster age) have a significant role in setting t_{eq} (actual nebula's age) of the ionized regions, which is mainly controlled by the electron temperature (given by the abundance). The effect is larger in low electron density environments. Their results give an average $t_{eq} \sim$ 13.6 Myr for an abundance of $Z = 0.0001$ ($\sim \frac{1}{170}$ $Z_\odot$, considering $Z_\odot = 0.017$) and $t_{eq} \sim$ 3.1 Myr for a metallicity of $Z = 0.0004$ ($\sim \frac{1}{44}$ $Z_\odot$). This implies that, at such low metallicity, there is a delay between the actual time when we observe the ionized region and the age of the stellar cluster responsible for this ionization. In practice, we would be observing low-metallicity regions apparently ionized by a young cluster, because of their emission-line spectrum, but we would not find any of the expected young, hot stars if we observed directly inside the nebula, just because the young star would have evolved. We would find more evolved stars instead producing, among other effects, a decrease of the values of the equivalent width, EW, of Balmer emission lines. This effect complicates considerably the determination of the physical properties of the stellar populations in XMDg. Finally, in very low-mass XMDg we could have mass segregation, which complicates even more the interpretation.

The previous paragraphs bring to light the fact that it is assumed that the metal content of an XMDg is the one derived from the ionized gas. A lot of hard work has been done by different groups to disentangle how do the gas abundance and the stars metallicity relate in these galaxies. This is a difficult matter introducing new biases and hypotheses when interpreting the data. Our approach to the solution involves running a photoionization code to compute the predicted emission-line spectrum, which can then be compared to the observations. The inputs for this code include the shape of the young cluster's ionizing spectrum (for which we utilize evolutionary stellar population synthesis models) and the assumptions regarding certain physical and chemical properties of the gas (see C22).

The characterization of older non-ionizing stellar populations from the observed visible spectrum poses a challenge due to the overwhelming presence of emission lines and the weak continuum. Nevertheless, the determination of the relative mass ratio of the most recent ionizing population to the entire stellar population, as well as the age of these constituents, can be approximated from the comparison of the observed equivalent widths of the Balmer lines with the theoretical values from synthesis stellar population models.

We would like to conclude this introduction by highlighting the main hypotheses that explain the origin of the low gas metal content in XMDgs. Three scenarios Ekta & Chengalur (2010) have been proposed to explain the lack of metals in these galaxies: (1) a genuinely low metal content, implying that the galaxy has always had a small amount of metals due to a very low star formation rate (SFR) throughout its history, preventing significant chemical enrichment; (2) dilution of the metals by the infall of pristine gas

from the outer disc, if present, or from the local environment, potentially as a result of an interaction with a neighbouring galaxy; and (3) a preferential loss of metals due to violent phenomena such as supernova (SN) events or outflows, like enriched galactic winds. We extensively discussed these scenarios in our paper on the Leoncino galaxy, AGC198691 (C22). These mechanisms are difficult to explore without studies of gas kinematics.

The progress in the understanding of XMDg demands new instruments for detailed spatially resolved studies (of both ionized gas and stellar populations properties throughout the galaxy) and moderate to high spectral resolution to analyse the gas kinematics. This implies obtaining 3D spectroscopy with the use of an Integral Field Unit (IFU); plus spectral resolution high enough to distinguish different gas kinematical components. These instruments allow to generate maps of the ionized gas, in different emission lines, obtaining its properties – electron density, electron temperature, ion abundances – at different galactocentric distances, and providing clues on the origin of the low metal content and the confinement (or not) of the ionized gas around the young clusters.

We are carrying out a programme to study nearby low-metallicity galaxies (most of them falling in the XMDg category) with the IFU of MEGARA (Multi Espectrógrafo en GTC de Alta Resolución para Astronomía) at the 10.4 m Gran Telescopio Canarias (GTC) in the Observatorio del Roque de los Muchachos (La Palma, Spain). MEGARA is an optical (3650–9750 Å) fibre-fed spectrograph offering two observing modes: IFU and multi-object spectroscopy. The IFU, with 623 fibres and a spatial sampling of 0.62 arcsec per fibre, provides a field of view (FoV) of 12.5×11.3 arcsec^2, plus eight additional mini-bundles, located at the edge of the FoV, for simultaneous sky subtraction. The spectrograph includes a set of 18 volume phase holographic (VPH) gratings, offering three spectral modes with resolving powers of $R_{\rm FWHM} \approx 6000$, 12 000, and 20 000 for low, medium, and high resolutions, respectively. The instrument description and performance on the GTC can be found in Carrasco et al. (2018) and Gil de Paz et al. (2018).

We have published MEGARA IFU observations of the XMD galaxy AGC198691, Leoncino (C22), with a spatial resolution of 22 pc spaxel^{-1} assuming a distance to the galaxy of 7.7 Mpc, and a spectral resolution of $R \sim$ 6 000. The oxygen abundance has been recently updated to 12 + log(O/H) = 7.06 (Aver et al. 2022). We did not find in our Leoncino observations any evidence of recent gas infall or loss of metals by means of outflows, pointing towards Leoncino being a genuine XMDg. Also, the extended observations of [O III] and Balmer lines throughout the ionized region demand photoionization by clusters of different ages, between 3.5 and 6.5 Myr that might respond to the evolution of a single cluster evolving along the cooling time of the nebula ($\sim$ 3 Myr at the metallicity of Leoncino, $Z = 0.0004$), to mass segregation of the cluster in smaller associations or a combination of these two phenomena.

This paper presents, for the first time, 3D spectroscopy of the galaxy SDSSJ0859 + 3923 (a system with a slightly higher abundance than Leoncino) obtained with the MEGARA IFU and the VPH gratings LR-B and LR-R, at a resolving power of $R \sim$ 6000, and similar spatial resolution (25 pc spaxel^{-1}). We analyse and discuss the results observed in five regions of ionized gas. Section 2 summarizes the published data of this galaxy; Section 3 presents our observations, data reduction, and analysis; the results are detailed in Section 4 and discussed in Section 5; and Section 6 summarizes the conclusions.

2 SDSSJ0859 + 3923 GALAXY

SDSSJ0859 + 3923 appears as a blue object in the SDSS catalogue (Abazajian et al. 2005). The SDSS *u*, *g*, *r*, *i*, and *z* magnitudes are 18.01, 17.05, 16.76, 16.62, and 16.57 mag, respectively. Prestwich et al. (2013) obtained FUV images from the *GALaxy Evolution EXplorer* (*GALEX*) catalogue (version 1.4.6), reporting very low reddening, $E(B-V) = 0.026$, and a value of $L_{\rm FUV}$ of 1.8×10^{47} erg s^{-1}, from which they derived an SFR of $1.72 \pm 0.02 \times 10^{-3}$ M$_\odot$ yr^{-1}. Brorby, Kaarret & Prestwich (2014) looked for X-ray sources in the 0.5–8 keV band with the back-illuminated ACIS-S3 chip aboard *Chandra* and for this galaxy found no source with $L_X > 2.272 \times 10^{38}$ erg s^{-1}, result confirmed by Douna et al. (2015). The galaxy was observed by Pustilnik & Martin (2016, hereafter PM16) in H I 21 cm transition with the Nançay Radio Telescope (NRT) as part of their sample of 45 galaxies in the Lynx-Cancer void. They gave a radial velocity of 586 ± 3 km s^{-1} from the H I line, assuming a distance of 11.4 Mpc and derived a total H I mass, $M_{\rm H\,I}$, of $1.84 \pm 0.27 \times 10^7$ M$_\odot$. Simultaneously, Thuan et al. (2016, hereafter T16) obtained H I observations with the 100 m Green Bank Telescope (GBT) of SDSSJ0859 + 3923, in their sample of 29 XMD star-forming blue compact dwarf galaxies. They reported for this galaxy a radial velocity 567 km s^{-1} from H I line (computed as the mid-point of the profile above 50 per cent of the line peak, v_{50}) and, adopting a distance of 10.2 Mpc, inferred a total $M_{\rm H\,I}$ of 2.0×10^7 M$_\odot$ within the large beam of the GBT at 21 cm. From a measured line width in the 21 cm line of $\Delta v_{50} = 39$ km s^{-1} and a extension of the H I-emitting region, computed as R(H I)$\sim 3\,R_g$, of 3×10.29 arcsec, they derived a dynamical mass, $M_{\rm dyn}$, of 2.88×10^8 M$_\odot$ and a ratio $M_{\rm H\,I}/M_{\rm dyn} = 0.069$. As the authors themselves point out, this estimate is highly uncertain, given that the derivation of $M_{\rm H\,I}$ relies on strong assumptions on R(H I) and on the nature of the H I 21 cm line broadening, which is assumed to be driven by random motions.

The *Hubble Space Telescope* (*HST*) *Barbara A. Mikulski Archive for Space Telescopes (MAST)* archive includes unpublished images (2017, proposal 12018, PI: Andrea H. Prestwich) obtained with WFC3-UVIS in the *F335W*, *F435W*, and *F606W* filters. We have used these data to correct the WCS solution of our MEGARA ground-based data using star-forming regions located both in the *HST* images and in our MEGARA reconstructed images (see Section 3). SDSSJ0859 + 3923 has an SDSS/DR14 (Data Release 14) spectrum (Abolfathi et al. 2018), used by I19 to include this galaxy as part of their sample of low-redshift ($z < 0.133$) XMD star-forming galaxies candidates, with oxygen abundance 12 + log(O/H) $\leq$ 7.35. I19 used DR14 coordinates, α (J2000.0 FK5) = 08$^{\rm h}$59$^{\rm m}$46$^{\rm s}$.93 and δ (J2000.0 FK5) = +39°23′05″.64, and a spectroscopic redshift of $z = 0.00200$, from which they inferred a distance of 8.95 Mpc, considering H$_0$ to be 67 km s^{-1} Mpc^{-1}. Data from SDSS give an integrated flux of Hβ in emission of 5.9×10^{-16} erg s^{-1}cm^{-2}, an equivalent width of Hβ of 28.3 Å and emission-line ratios values for [O III]4363/Hβ, [O III]4959/Hβ, [N II]6584/Hβ, and [O II]7325/Hβ of 0.086, 0.438, 0.091, and 0.065, respectively. The [O II]3727, 3729 lines were not available in SDSS spectra, but I19 estimated [O II]3727, 3729/Hβ = 1.989 based on the relationship between these lines and the [O II]7325 line. They gave a direct oxygen abundance of 12 + log(O/H) = 7.35 (equivalent to $\sim \frac{1}{22}$ Z$_\odot$), and estimated a value of the stellar mass, M_*, of $\approx 2.51 \times 10^5$ M$_\odot$. We will use all these published data in the discussion (Section 5).

Table 1. MEGARA spectral configurations used in the observations of SDSSJ0859 + 3923. The description of the columns is given in Section 3. The range between λ_{min} and λ_{max} is common to all fibres, but the widest one between λ^{1}_{min} and λ^{1}_{max} is the one obtained at least with one fibre.

VPH	λ^{1}_{min} (Å)	λ_{min} (Å)	λ_{c} (Å)	λ_{max} (Å)	λ^{1}_{max} (Å)	$\delta\lambda$ (Å pix^{-1})
LR-B	4321.63	4332.44	4777.15	5221.85	5231.28	0.221
LR-R	6091.69	6097.27	6721.30	7345.33	7349.98	0.307

Table 2. Observations details of SDSSJ0859 + 3923 with MEGARA at the GTC. The pointing coordinates are included in Section 3. Position angle was 0°.

	Obs 1	Obs 2	Obs 3
VPH	LR-B	LR-B	LR-R
Date	20/12/2019	20/12/2019	24/12/2019
OB ID	0005	0006	0007
N x texp (s)	3 × 1800	3 × 1800	3 × 1800
Hour (UT), start	01:51:57.94	03:26:08.15	02:13:58.24
Hour (UT), end	02:54:26.67	04:28:36.75	03:16:26.85
Flux star	HR3454	HR3454	HR1544
Seeing (arcsec)	1.2	0.9	1.2
Airmass	1.180–1.067	1.036–1.018	1.103–1.032
Cloud	Clear	Clear	Clear
Moon	Grey	Grey	Dark

3 MEGARA OBSERVATIONS AND DATA ANALYSIS

We have obtained IFU observations of the galaxy SDSSJ0859 + 3923 with MEGARA on the GTC 10.4-m telescope. The data were taken with the LR-B and LR-R VPH gratings. Table 1 summarizes the wavelength range and spectral sampling obtained after wavelength calibration for each set-up. The columns indicate (1) set-up (VPH label); (2) the shortest wavelength (Å) seen at least in one fibre; (3) the shortest wavelength (Å) seen in all fibre spectra; (4) central wavelength (Å); (5) the longest wavelength (Å) seen in all fibre spectra; (6) the longest wavelength (Å) seen at least in one fibre; and (7) linear reciprocal dispersion in Å pix^{-1}.

The MEGARA-IFU observations presented in this work have an unprecedented simultaneous spatial (0.62 arcsec spaxel^{-1}) and spectral resolution ($R_{FWHM} \approx 6\,000$). The data were taken under GTC6-19BGMEG programme in December 2019 and January 2020, in grey/dark nights under clear conditions in terms of atmospheric transparency. The observations are summarized in Table 2. The observing time was divided into three identical exposures to facilitate cosmic rays removal. The associated daytime calibrations were bias, halogen and spectral lamps (ThAr for LR-B and ThNe for LR-R), used for bias subtraction, fibre tracing and flat field correction, and wavelength calibration, respectively. Night-time observations of spectrophotometric standard stars were made to generate the response function for absolute flux calibration. The data were reduced with the MEGARA Data Reduction Pipeline (DRP), a PYTHON-based software tool operating in command line (Cardiel & Pascual 2018; Pascual et al. 2018).

The resulting product of the DRP is a row-stacked spectra (RSS) 2D FITS file, which contains the individual flux-calibrated 1D spectra for all 623 IFU fibres. The DRP also produces a final RSS file in which the sky has been subtracted by combining the signal of up to eight sky mini-bundles placed along the IFU pseudo-slit. Alternatively, a customized sky average of the desired fibres can be subtracted using the Quick Look Analysis (QLA) tool (Gómez-Alvarez et al. 2018). This software package also provides the visualization of the recombined image from the fibre RSS spectra in the desired spectral window, among many other functionalities.

The target coordinates used to point GTC/MEGARA were α (J2000.0 FK5) = $08^{h}59^{m}47\overset{s}{.}048$ and δ (J2000.0 FK5) = $+39°23'04\overset{''}{.}709$. From the comparison of the *HST* clusters with MEGARA ionized regions coordinates, we derived the shifts between the *HST F*448*W* image and MEGARA LR-B pointing and between the *HST F*606*W* image and LR-R. The headers of the corresponding MEGARA synthetic images were updated to match the *HST* WCS solution. In this regard, the availability of *HST* imaging was crucial as there were no stars within the field of MEGARA IFU. Thus, the main source of information come from the comparison of the location of the different line-emitting regions found in Hα and Hβ identified through our LR-B and LR-R observations and the brightest regions in the *HST F*448*W* and *F*606*W* filters, respectively. Note that these two filters include bright emission lines that dominate the image counts in the high surface brightness regions within the galaxy. Fig. 1 shows some emission line flux contours overlapped on *HST* archive WFC3 images for the spaxels with measured S/N > 5 in every line involved (293, 202, and 225 spaxels for Hα, Hβ, and [O III] 5007, respectively). Based on this comparison with *HST* images, we estimate that our alignment precision is better than half a spaxel (∼0.3 arcsec), for both LR-B and LR-R set-up. Relative to the GTC telescope absolute pointing coordinates, LR-B turned out to be offset by 1.7 arcsec in right ascension and −1.2 arcsec in declination, while LR-R was offset by 1.1 arcsec in right ascension and −1.0 arcsec. The corresponding astrometric correction was applied to all the results in this paper involving absolute positions (e.g. maps or comparison of the MEGARA-IFU and *HST* morphology). This includes the coordinates provided for the five brightest emission-line regions identified in our data, which are listed in Table 3, and that has been marked in the panels (a) of Fig. 1 with crosses, and labelled in the panels (b) of the same figure with the letters.

We adopt a spectroscopic redshift of $z = 0.00198$, which for $H_0 = 67\,km\,s^{-1}Mpc^{-1}$ yields a distance of 8.5 Mpc, a spaxel size of 25 pc and a FoV on MEGARA IFU of 505 pc × 456 pc. Absolute quantities (luminosities, masses) published in the literature have been scaled to the distance adopted in this paper. The values for PM16, T16, I19, and this work are as follows, respectively: (a) distances are 11.6, 10.2, 8.95, and 8.5 Mpc; (b) MEGARA spaxel sizes are ∼34, 30, 26, and 25 pc; (c) the scale factors for the galactocentric distance (relative to this work) are 1.36, 1.20, 1.04, and 1.00 while for (d) mass (except for the dynamical mass that scales linearly with distance) or luminosity relative to the values used in this work are 1.86, 1.44, 1.11, and 1.00.

4 RESULTS

4.1 Ionized gas: distribution and kinematics

The left panels in Fig. 1 present the contours overlapped on *F*336*W* *HST* images, while the right ones show the same contours but overlapped on *F*606*W* (top row) and *F*438*W* (middle and bottom rows) *HST* images. The images display fluxes of Hα (top), Hβ (middle), and [O III] 5007 (bottom) emission lines in units of e^{-} s^{-1}. In the top-left panel (Fig. 1a), we show the location of the five H II regions identified in our brightest emission-line images (Hα, as well as [O III] 5007), while they are labelled in panel 1(b). The coordinates of these regions are provided in Table 3. A comparison of the locations of these regions with the deepest *F*606*W* *HST* image

Table 3. Coordinates of the H II regions in SDSSJ0859 + 3923 identified in our MEGARA synthetic H α images.

Region	α (J2000.0 FK5)	δ (J2000.0 FK5)
A	$08^h59^m47^s.22$	$+39°23'07''.12$
B	$08^h59^m46^s.90$	$+39°23'04''.97$
C	$08^h59^m46^s.96$	$+39°23'01''.81$
D	$08^h59^m47^s.12$	$+39°23'04''.50$
E	$08^h59^m47^s.35$	$+39°23'04''.80$

reveals that regions labelled B, C, and D are situated in areas where the continuum is strongest, including emission from underlying stellar populations, while regions A and E exhibit comparatively fainter underlying continuum emission.

The panels showing UV (*F*336*W*) and optical-blue (*F*438*W*) images allow for a comparison between the ionized regions and the UV continuum sources. On one hand, regions A, C, and E appear to have only a single unresolved bright UV-blue source associated with them, possibly responsible for the ionizing flux that leads to the line emission detected in these regions. On the other hand, region D seems to be associated with a diffuse UV-bright area, possibly an overlap of several individual stars, while region B hosts several UV-bright regions nearby, none of which align with the position of the brightest spaxels detected in line emission. The brightest UV source is located 1 arcsec north of the brightest spaxel of the H II region). This suggests that, in this latter region, there may be spatial segregation between the ionized gas and the ionizing stars, or there may be a more evolved, more massive cluster capable of producing a similar amount of ionizing photons. However, a very young ionizing cluster is still required to account for the excitation observed in the emission-line spectrum. This figure also shows that region A has the highest [O III] 5007/Hβ ratio, even though region C has the brightest UV emission (consistent with the mass of the ionizing clusters estimated in Section 5.1). There are three possible explanations for this: either *F*336*W* and *F*438*W* flux cannot tell the difference between the actual ionizing flux of the sources present in these clusters, or regions A and C have different ages and possibly different masses of young ionizing clusters, which could explain both the difference in excitation and the number of ionizing photons. The latter explanation is consistent with the properties we derived for the ionizing clusters responsible for the emission-line spectra of the different regions using POPSTAR + CLOUDY models (see Section 5). However, the stochastic effects are not negligible due to the small young cluster's masses, between 5×10^2 and 2×10^3 $M_\odot$, derived from the number of ionizing photons for regions A, B, C, and D.

Fig. 2 shows the maps of the different measurements derived from the analysis of the H α (left) and H β (right) lines obtained from MEGARA LR-R and LR-B images, respectively. These panels display the flux in $\times\,10^{-17}$ erg s^{-1} cm^{-2} (top), the radial velocity in km s^{-1} (middle), and the velocity dispersion in km s^{-1} (bottom). The Hβ intensity image is the one where the five H II regions are best isolated. A faint peak in Hβ emission is also found 3 arcsec NW of region B but because it is only marginally brighter that its surroundings and it is not obvious in any other emission line, we have not analysed it as an additional isolated H II region.

Panel 2(c) shows a complicated line-of-sight radial velocity field. In order to interpret this map, we recall that not only regions B and C are very bright but are also located in regions of strong underlying continuum emission. Therefore, it seems reasonable to assume that the part of the velocity field aligned with those two regions, where a clear velocity gradient is observed (with an amplitude of $\sim$20 km s^{-1}), traces the bulk of the dynamical mass of the galaxy within the central few hundred parsecs. In addition to the previously mentioned NW-SE velocity gradient, we find that regions A and E do not follow the same regular radial velocity pattern. Since these two regions are located at the edge of the galaxy's main body, as traced by the *F*606*W* continuum, we propose that they represent gas clouds currently falling into the galaxy's shallow gravitational potential, thereby retaining much of their peculiar radial motions.

Fig. 3 shows in the top panels the flux (in erg s^{-1} cm^{-2}) of [O III] 5007 emission line at the left, and the ratio [O III] 5007/Hβ at the right. As commented above, region A shows the highest [O III] 5007/Hβ despite not having the brightest F336W source associated to it. The bottom panels display the radial velocity (in km s^{-1}) and velocity dispersion (in km s^{-1}) of [O III] 5007.

Fig. 2(e), Fig. 2(f), and Fig. 3(d) show the velocity dispersion maps in H α, H β, and [O III] 5007, respectively. The analysis of the arc lines used for wavelength calibration in both spectral set-ups (LR-B and LR-R) indicates that the instrumental line profile can be adopted as a Gaussian within our measurement errors. Therefore, the measured velocity dispersions (in km s^{-1}) have been corrected for instrumental broadening using the average resolving power in FWHM measured at the wavelength of the corresponding line from the interpolated image quality maps, derived by the MEGARA DRP, and subtracting quadratically the instrumental sigma (c/2.35/R) from the corresponding observed values. Although the average spectral resolution in both set-ups is $R_{\rm FWHM} \approx 6000$, we obtained differences noticeable enough to make the instrumental sigma to vary between 20.3 km s^{-1} for [O III] 5007, 20.4 km s^{-1} for H β, and 23.6 km s^{-1} for H α. In addition, variation in image quality across the field can introduce an error of 1 km s^{-1} in the instrumental velocity dispersion, which implies that corrected velocity dispersions below 5 km s^{-1} are uncertain.

We derive velocity dispersion values (corrected for instrumental broadening) of the order of 10 km s^{-1}, except for region D, where the velocity dispersion peaks at 30–40 km s^{-1}. The low cluster masses involved suggest that specific events in the evolution of stars within these clusters can have a significant impact on their overall properties. The unusually high velocity dispersion observed in region D could be related to, among other factors, the presence of massive stellar winds or a recent type-II SN explosion. Fig. 4 shows the velocity dispersion gradient in region D, representing in different colours the values obtained from H β (blue), [O III] 5007/ (green), and H α (red) images.

In Fig. 5, we present the contours of different velocity channels around Hα overlaid on the *F*606*W* WFC3-UVIS/*HST* image of the galaxy. Each panel corresponds to a different wavelength, as determined by the final linear solution of our MEGARA LR-R (topocentric) wavelength-calibrated data. The velocity channels correspond to emissions at 6573.1, 6573.4, 6574.0, 6574.4, 6574.7, 6575.0, 6575.3, and 6575.7 Å as labelled from left to right and top to bottom in the panels. Although region D, along with region E, is the faintest of all H II regions identified, we observe emission from it in all panels except for panel 5(h), likely due to its larger velocity dispersion. Given the low-velocity amplitude of the motions detected in the line emission of the object ($\sim$20 km s^{-1}), which is comparable to the instrumental resolution (23.6 km s^{-1} for H α), and the reciprocal dispersion of the data ($\sim$0.3 Å pixel^{-1}, corresponding to a velocity difference of 11 km s^{-1}) between consecutive panels, the contours for all regions except D primarily reflect differences in H α line intensity across the different regions in the galaxy.

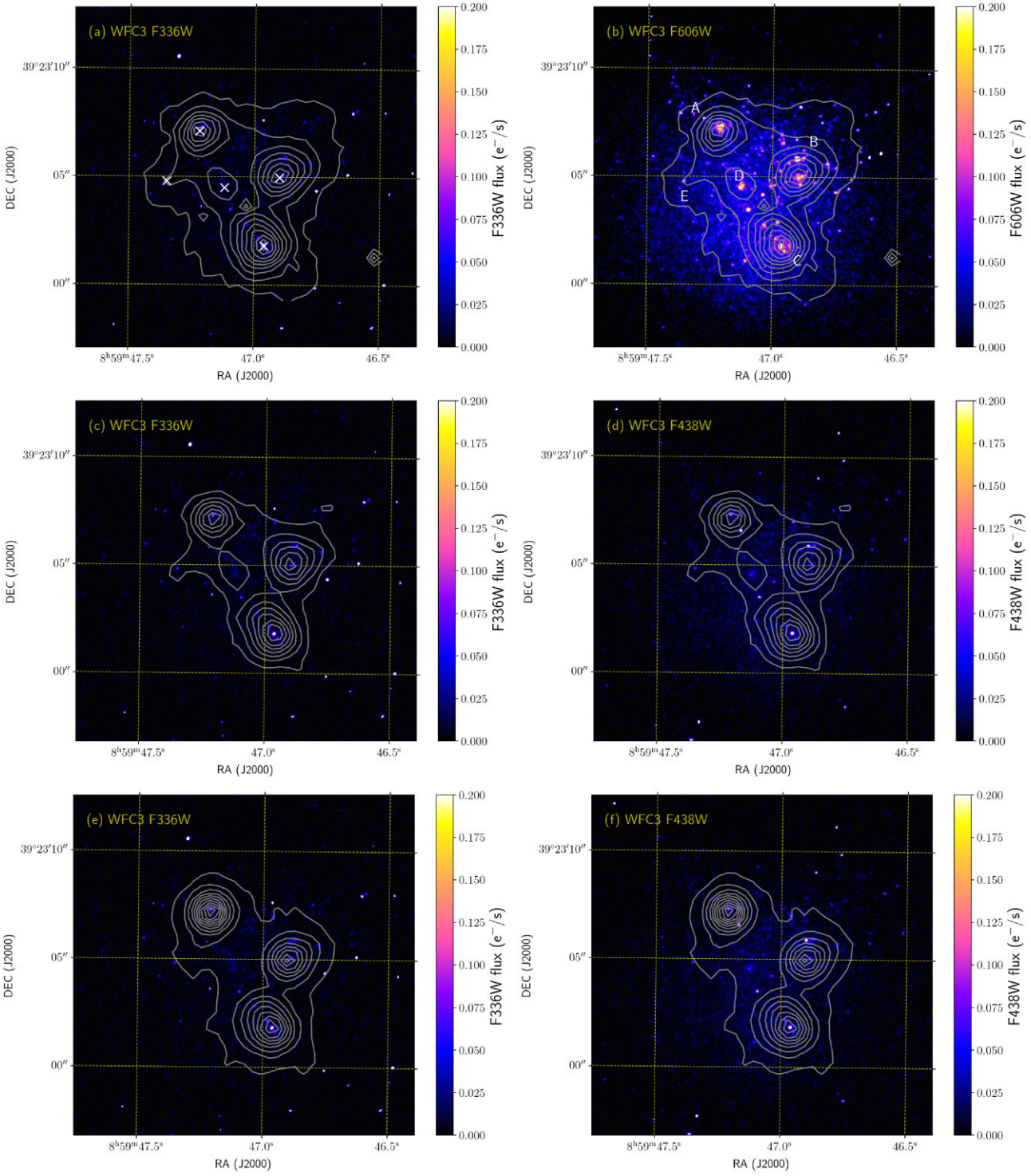

Figure 1. MEGARA emission lines contours overlapped on *HST* archive WFC3 images. Top panels: H α flux contours on *F*335*W* (left) and *F*606*W* (right) WFC3 images. Middle panels: H β flux contours on *F*335*W* (left) and *F*438*W* (right). Bottom panels: [O III] 5007 flux contours on *F*335*W* (left) and *F*438*W* (right). The contours range from 5×10^{-18} erg s^{-1} cm^{-2} (per spaxel) to $9\times10^{-16}/3.5\times10^{-16}/3.5\times10^{-16}$ erg s^{-1} cm^{-2} in steps of $10^{-17}/5\times10^{-18}/10^{-17}$ erg s^{-1} cm^{-2}, respectively, for H α, Hβ, and [O III] 5007. The units in the *HST* images (in electrons s^{-1}) can be converted to flux density, f_ν, in Jy, by using the corresponding PHOTFNU keyword for each WFC3 filter, namely 4.83×10^{-7}, 4.23×10^{-7}, and 1.34×10^{-7} Jy/(e$^-$ s^{-1}), respectively, for *F*335*W*, *F*438*W*, and *F*606*W*. In terms of f_λ, the conversion is given by the corresponding PHOTFLAM keyword, namely 1.287×10^{-18}, 6.78×10^{-19}, and 1.157×10^{-19} erg cm^{-2} Å^{-1}/e$^-$.

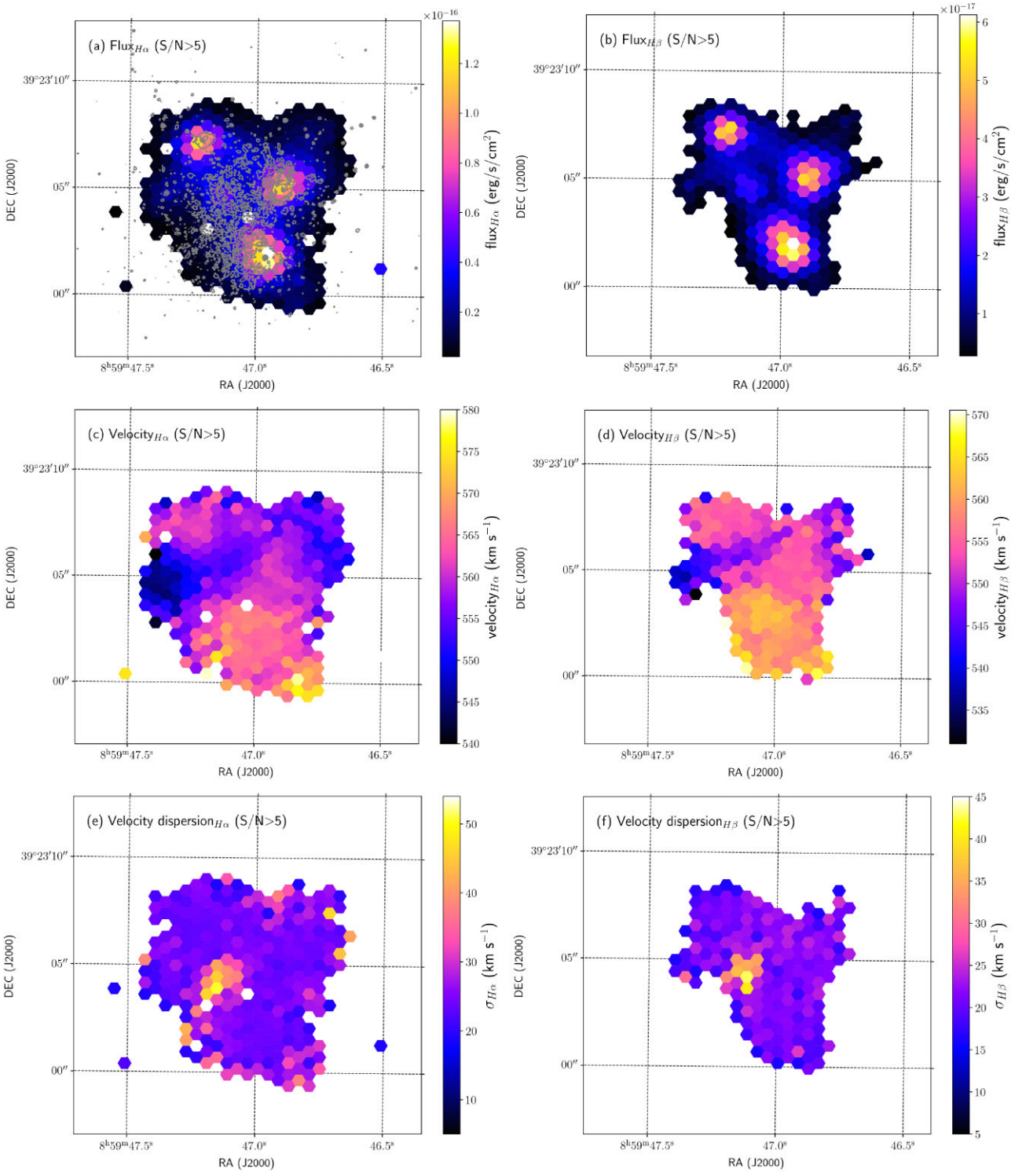

Figure 2. Left: Maps of H α obtained from MEGARA LR-R: flux in $\times\ 10^{-17}$ erg s^{-1} cm^{-2} (top), radial velocity in km s^{-1} (middle), and velocity dispersion in km s^{-1}(bottom). Right: Same maps and units for H β, obtained from MEGARA LR-B: flux (top), radial velocity (middle), and velocity dispersion (bottom). The instrumental sigmas for H β and for H α are 20.4 and 23.6 km s^{-1}, respectively. The contours in panel (a) come from the *HST* archival image obtained with the WFC3-UVIS/*HST* instrument in the *F606W* band and correspond to 0.05, 0.15, 0.25, 0.35, 0.45, 0.55, 0.65, 0.75, 0.85, and 0.95 electrons s^{-1} or 0.6, 1.7, 2.9, 4.0, 5.2, 6.4, 7.5, 8.7, 9.8, and 11.0 $\times\ 10^{-20}$ erg s^{-1} cm^{-2} Å^{-1}.

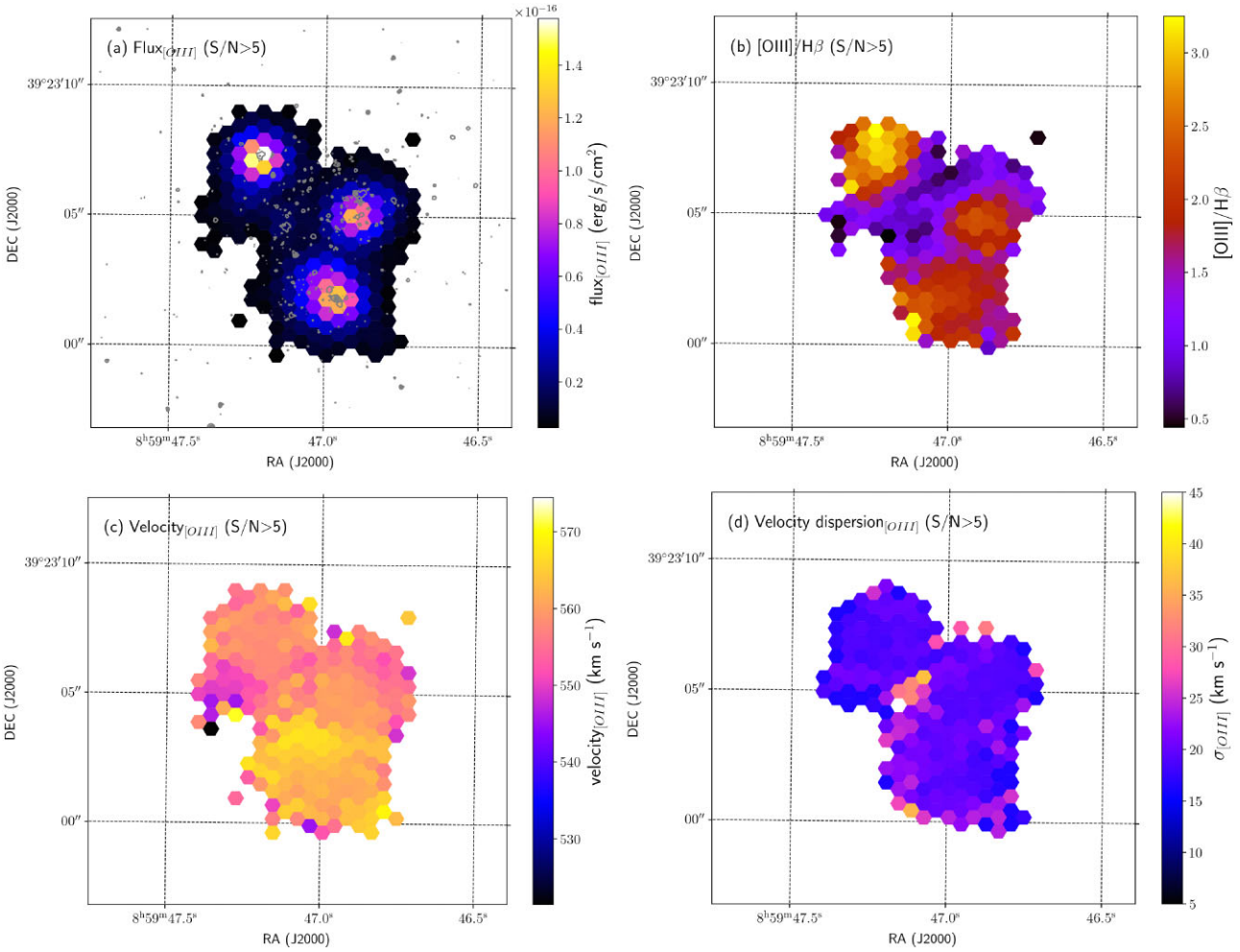

Figure 3. Top left: Maps of [O III] 5007 flux (in erg s^{-1} cm^{-2}). Top-right: Map of the emission line ratio [O III] 5007/Hβ. Bottom left: Velocity (in km s^{-1}) of [O III] 5007. Bottom right: Velocity dispersion (in km s^{-1}) of [O III] 5007. The instrumental sigmas for [O III] 5007 is 20.3 km s^{-1}. The contours in panel (a) come from the *HST* archival image obtained with the WFC3-UVIS/*HST* instrument in the *F*438*W* band and correspond to 0.03, 0.13, 0.23, 0.33, 0.43, 0.53, 0.63, 0.73, and 0.83 electrons s^{-1} or 0.2, 0.9, 1.6, 2.2, 2.9, 3.6, 4.3, 4.9, and 5.6 $\times 10^{-19}$ erg s^{-1} cm^{-2} Å^{-1}.

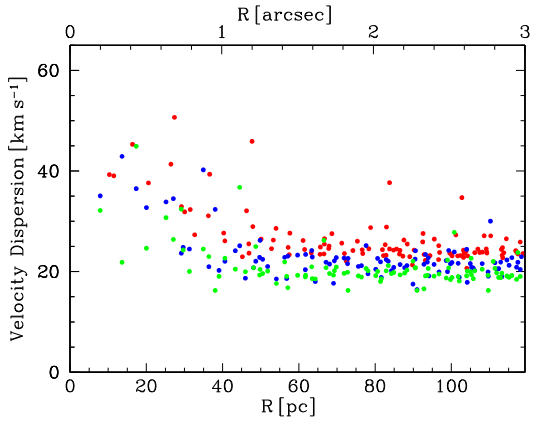

Figure 4. Radial gradient of velocity dispersion (sigma), corrected from the instrumental sigma, as a function of the distance from the central spaxel of region D. We have represented all spaxels and used three colours: blue for Hβ, green for [O III] 5007, and red for Hα. Instrumental sigmas for Hβ, [O III] 5007, and Hα are 20.4, 20.3, and 23.6 km s^{-1}, respectively.

4.2 Gas emission lines throughout the ionized region

In this section, we examine the properties of the four ionized regions identified in the galaxy, labelled A, B, C, and D. Fig. 2 (for Hα and Hβ) and Fig. 3 (for [O III] 5007 and [O III] 5007/Hβ) display the flux maps of the most prominent emission lines from the MEGARA data. Fig. 6 shows the equivalent-width maps of Hα (top) and Hβ (bottom), obtained from MEGARA LR-R and LR-B reconstructed images, respectively.

4.2.1 The aperture effect

We measured the emission lines in spectra extracted using different circular apertures, each corresponding to a specific slit width. The inner aperture has an radius of 12.5 pc for all regions, while the outer aperture, encompassing the entire detectable ionized region, has a radius of 87.5 pc for regions A, B, and C, and 62.5 pc for region D. The results are presented in Table 4 for LR-B and Table 5 for LR-R. The first four columns are identical in both tables: (1) the distance from the central brightest spaxel to the edge of the extracted aperture in arcsec; (2) the corresponding distance, in pc;(3) the outermost ring with ionized gas emission included within the

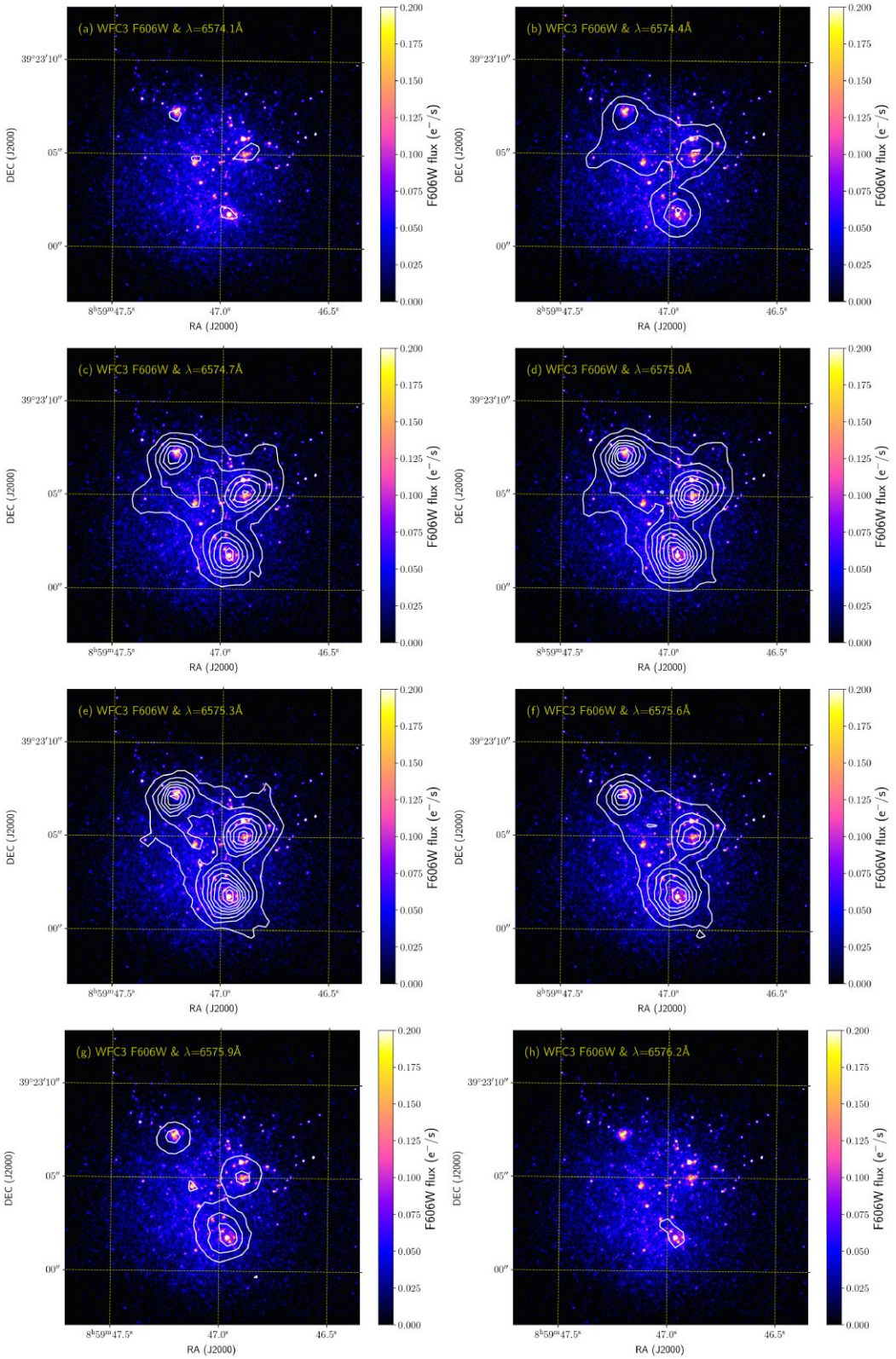

Figure 5. WFC3-UVIS/*HST F*606*W* image on which we have overlapped the velocity channels around Hα line, as described in Section 4.1. The contours shown correspond to surface brightness values ranging from 1×10^{-5} to 5×10^{-4} in intervals of 10^{-5} Jy paxel^{-1}.

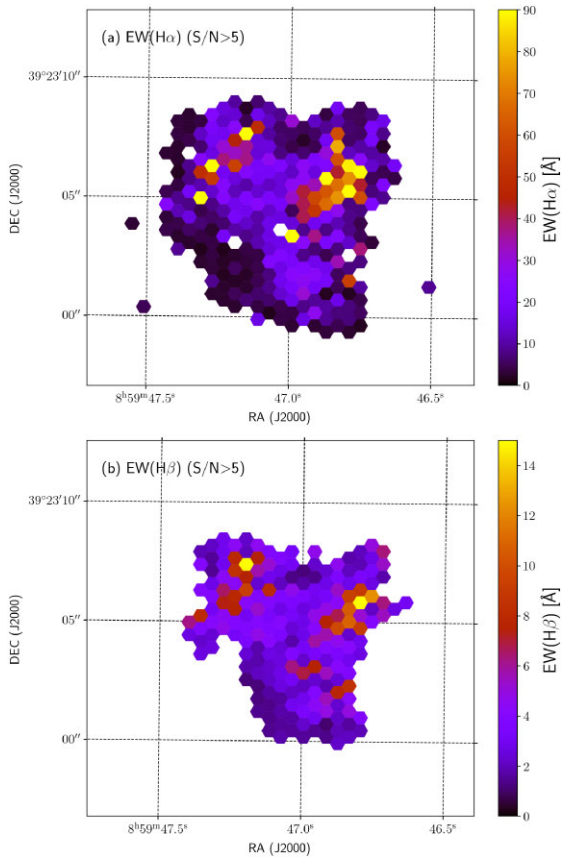

Figure 6. Maps of the equivalent width (in Å) of H α (top) and Hβ (bottom) measured in all spaxels with S/N larger than 5 from MEGARA LR-R and LR-B data, respectively. The relatively low values indicate the existence of an underlying population much older than the young clusters responsible for the ionization.

aperture, with 0 representing the central spaxel and a separation of 25 pc between consecutive apertures; and (4) the number of spaxels included in the spectrum for that aperture. The rest of the columns display the fluxes in each aperture for the strongest lines in units of 10^{-17} erg s^{-1} cm^{-2}. Table 4 gives the H γ flux, equivalent width of H γ, H β flux, equivalent width of H β; and the fluxes of [O III] 4959 Å and [O III] 5007 Å in columns 5–10. Table 5 contains (in columns 5–10) the H α flux, equivalent width of H α; and the fluxes of [N II] 6584 Å, [S II] 6717 Å, [S II] 6731 Å, and [Ar III] 7135 Å. We identified the [He I] 5015 Å and [N II] 6548 Å, emission lines in few spaxels of regions A, B, and C and we detected the [He II] 4686 Å, line faintly in region A alone. However, the signal is low, SNR < 5 in all cases, and the errors are too large to extract a reliable measurement.

We have also measured the [O III] 4363 Å but only for the full aperture of region A. The flux is $(6.8 \pm 2.5) \times 10^{-17}$ erg s^{-1} cm^{-2}. We used the [O III] 4363 Å flux in region A to estimate the electron temperature (T_e) of the gas and the oxygen abundance. Unfortunately, our data do not permit precise line flux measurements of [O III] 4363 Å in the other regions due to the intrinsically weak signal of the line and its position at the bluest edge of the VPH spectral range, where grating transmission drops. Additional GTC observing time has been requested using the MEGARA LR-U set-up, which will enable further complementary observations for this study in the future.

We performed an absolute flux calibration using spectrophotometric standard stars. However, since the nights were not entirely photometric, we observed flux differences between the LR-B set-up (all observing blocks conducted on the same night) and the LR-R set-up (observed on a different night), which are analysed below. We verified that the Hβ emission flux from SDSS DR14 observations centred near our region B, 5.9×10^{-16} erg s^{-1} cm^{-2}, is in good agreement with our measured value for that region using a synthetic 1.6 arcsec-radius aperture, $(5.4 \pm 0.1) \times 10^{-16}$ erg s^{-1} cm^{-2}, validating the absolute fluxes in the LR-B set-up.

We compared the observed flux ratio of H γ to H β (both in the LR-B spectra) with theoretical values predicted for an electron temperature consistent with the average metallicity of the regions. I19 derived a value of 12 + log(O/H) = 7.35 from SDSS DR14 data, equivalent to $\sim \frac{1}{22}$ or $Z = 0.001$). Using the total aperture, we integrated the fluxes across the entire ionized regions to derive the dust reddening, following the equation provided by Calzetti, Kinney & Storchi-Bergmann (1994, and references therein):

$$\log \frac{F(\mathrm{H}\,\gamma)}{F(\mathrm{H}\,\beta)} = \log 0.474 - 0.4 \times \frac{A_v}{R}(k(\mathrm{H}\,\gamma) - k(\mathrm{H}\,\beta)), \qquad (1)$$

where $F(\mathrm{H}\,\gamma)$ and $F(\mathrm{H}\,\beta)$ are the observed fluxes of H γ and H β, respectively, the value 0.474 (Osterbrock 1989) is the theoretical ratio for an electron temperature of 20 000 K; $k(\mathrm{H}\gamma)$ and $k(\mathrm{H}\beta)$ are the values from the extinction curve. We have used the extinction curves for star-forming regions (Calzetti 1999) and for LMC (Howarth 1983) to derive $E(B-V) = A_V/R$. We obtain null reddening corrections for regions A, B, and C, and a value of $E(B-V) = 0.4$ (Calzetti 1999) or 0.2 mag (Howarth 1983) for region D.

Fig. 7 presents the values of several emission line ratios: [O III] 5007/Hβ (top left), [N II] 6584/H α (top right), [S II]6716, 6731/H α (bottom left), and [Ar III] 7135/H α (bottom right), as a function of the integrated aperture size. The ratios were chosen so emission lines within the same set-up are used: LR-B for panel (a) and LR-R for panels (b), (c), and (d), to minimize the impact of absolute flux calibration errors. We examined the *aperture effects*, how the emission lines vary with different extraction aperture sizes within the same ionized region. We reported this effect, for the first time in these type of galaxies, in Leoncino (C22) and we are further investigating it in a sample of XMD galaxies observed with the MEGARA IFU.

Fig. 7 (a) shows the aperture effect for the high-excitation regions A, B, and C, where the value of [O III] 5007/Hβ decreases as the aperture size increases. The ratio of the fluxes for the total aperture (entire region) decreases to 40 per cent for region A, 42 per cent for region B, and 14 per cent for region C compared to the values within the central small aperture, with [O III] 5007 Å flux declining more rapidly than Hβ flux as the aperture size increases. We found this same aperture effect in Leoncino galaxy (C22). If this trend is confirmed, the size of the observed region could represent another source of bias: candidates for XMD galaxies have been identified in surveys as those with the highest [O III] 5007/Hβ ratios, but the long-slit observations in these surveys (e.g. SDSS) use a fixed and relatively large fibre size ($\sim$ 2 arcsec), and often capture the emission from the entire region, potentially masking the fact that [O III] 5007/Hβ ratios are lower across the whole region than in the central area. This could result in many candidates being overlooked. Our preliminary results indicate that this aperture effect is more pronounced for lower-metallicity galaxies, with larger aperture effects occurring in more compact or distant galaxies where the entire ionized region falls within the fixed slit width or fibre-core size. Region D does not exhibit any aperture effect, as it has a small size, a much lower [O III] 5007/Hβ ratio, low equivalent width of Balmer lines, and distinctively high σ values (see subSection 4.1).

Table 4. LR-B emission lines measurements in different integrated apertures from the central brightest spaxel for each of the four ionized regions labelled as A, B, C, and D. Fluxes are given in units of $\times 10^{-17}$ erg s^{-1} cm^{-2} and equivalent widths in Å. Fluxes in this table are not corrected for dust reddening.

(1) d arcsec	(2) d pc	(3) nr	(4) Ns	(5) Hγ Flux	(6) Hγ EW	(7) Hβ Flux	(8) Hβ EW	(9) [O III]4959 Flux	(10) [O III]5007 Flux
Region A									
0.3	12.5	c	1	2.294 ± 0.627	10.23 ± 5.38	5.212 ± 0.524	95.79 ± 64.88	5.260 ± 0.513	15.770 ± 0.912
0.9	37.5	1	7	12.280 ± 1.446	5.97 ± 1.06	26.530 ± 1.061	34.14 ± 5.41	26.070 ± 0.992	77.330 ± 1.632
1.6	62.5	2	19	26.100 ± 3.152	6.90 ± 1.34	47.230 ± 1.405	20.89 ± 1.91	43.600 ± 1.627	129.900 ± 2.368
2.2	87.5	3	37	41.610 ± 9.143	7.52 ± 2.76	63.180 ± 1.868	15.44 ± 1.20	53.040 ± 1.867	158.500 ± 2.792
Region B									
0.3	12.5	c	1	2.890 ± 0.544	9.26 ± 3.07	5.174 ± 0.339	51.60 ± 16.59	3.843 ± 0.320	12.080 ± 0.487
0.9	37.5	1	7	13.850 ± 1.714	6.38 ± 1.18	27.410 ± 0.848	35.87 ± 4.51	19.420 ± 0.679	58.660 ± 1.050
1.6	62.5	2	19	27.900 ± 2.545	4.56 ± 0.55	54.420 ± 1.282	25.87 ± 2.09	34.380 ± 1.039	103.700 ± 1.679
2.2	87.5	3	37	37.590 ± 4.039	3.36 ± 0.44	79.010 ± 1.867	20.73 ± 1.50	44.690 ± 1.412	136.700 ± 2.603
Region C									
0.3	12.5	c	1	3.577 ± 0.587	14.52 ± 5.47	6.149 ± 0.346	31.68 ± 6.80	4.159 ± 0.244	12.530 ± 0.451
0.9	37.5	1	7	17.950 ± 2.251	6.19 ± 1.19	34.710 ± 0.932	22.50 ± 1.93	22.750 ± 0.764	69.280 ± 1.356
1.6	62.5	2	19	40.440 ± 10.570	8.72 ± 4.07	69.340 ± 1.412	21.78 ± 1.39	44.820 ± 1.279	134.500 ± 2.123
2.2	87.5	3	37	63.130 ± 19.880	9.55 ± 5.60	95.390 ± 1.982	17.37 ± 1.01	60.280 ± 1.717	180.200 ± 2.818
Region D									
0.3	12.5	c	1	0.935 ± 0.486	3.61 ± 2.31	1.634 ± 0.231	17.54 ± 6.95	0.522 ± 0.153	1.228 ± 0.166
0.9	37.5	1	7	3.948 ± 1.216	1.78 ± 0.59	10.160 ± 0.605	14.86 ± 2.28	2.676 ± 0.381	8.041 ± 0.535
1.6	62.5	2	19	10.090 ± 2.580	1.50 ± 0.41	23.080 ± 0.948	11.92 ± 1.12	7.267 ± 0.832	20.270 ± 1.028

Table 5. LR-R emission lines measurements in different integrated apertures from the central brightest spaxel for each of the four ionized regions labelled as A, B, C, and D. Fluxes are given in units of $\times 10^{-17}$ erg s^{-1} cm^{-2} and equivalent width in Å. Fluxes in this table are not corrected for dust reddening.

(1) d arcsec	(2) d pc	(3) nr	(4) Ns	(5) Hα Flux	(6) Hα EW	(7) [N II]6584 Flux	(8) [S II]6716 Flux	(9) [S II]6731 Flux	(10) [Ar III]7135 Flux
Region A									
0.3	12.5	c	1	11.670 ± 0.504	118.85 ± 31.39	0.293 ± 0.114	0.558 ± 0.141	0.367 ± 0.119	–
0.9	37.5	1	7	59.240 ± 1.457	92.05 ± 12.16	1.735 ± 0.335	3.135 ± 0.365	2.644 ± 0.341	1.107 ± 0.533
1.6	62.5	2	19	105.700 ± 2.544	80.51 ± 9.71	3.296 ± 0.608	6.885 ± 0.644	5.290 ± 0.584	1.948 ± 0.823
2.2	87.5	3	37	142.100 ± 3.156	55.16 ± 5.05	3.990 ± 1.026	10.690 ± 1.013	8.349 ± 0.919	2.690 ± 1.175
Region B									
0.3	12.5	c	1	11.440 ± 0.609	161.96 ± 61.7	0.250 ± 0.095	0.893 ± 0.137	0.597 ± 0.115	0.163 ± 0.105
0.9	37.5	1	7	63.960 ± 1.633	132.73 ± 21.93	1.778 ± 0.323	5.803 ± 0.493	3.944 ± 0.419	0.813 ± 0.363
1.6	62.5	2	19	126.200 ± 2.779	99.77 ± 11.32	3.696 ± 0.575	12.300 ± 0.883	8.477 ± 0.759	–
2.2	87.5	3	37	184.500 ± 3.753	77.73 ± 7.78	5.992 ± 1.732	20.010 ± 1.311	13.300 ± 1.125	–
Region C									
0.3	12.5	c	1	13.650 ± 0.454	112.53 ± 22.25	0.238 ± 0.110	0.837 ± 0.132	0.539 ± 0.114	0.292 ± 0.127
0.9	37.5	1	7	75.660 ± 1.470	92.97 ± 9.75	1.624 ± 0.319	4.375 ± 0.380	3.232 ± 0.344	1.514 ± 0.578
1.6	62.5	2	19	151.400 ± 2.395	75.86 ± 5.83	3.394 ± 0.537	9.657 ± 0.730	6.797 ± 0.648	2.022 ± 1.036
2.2	87.5	3	37	218.200 ± 3.414	61.95 ± 4.24	5.561 ± 0.862	14.430 ± 1.022	10.440 ± 0.916	3.949 ± 1.445
Region D									
0.3	12.5	c	1	4.272 ± 0.348	53.74 ± 17.82	0.150 ± 0.095	0.773 ± 0.144	0.446 ± 0.118	–
0.9	37.5	1	7	24.670 ± 1.252	38.33 ± 6.64	0.850 ± 0.283	4.086 ± 0.378	2.718 ± 0.326	–
1.6	62.5	2	19	59.390 ± 2.160	38.09 ± 4.71	1.762 ± 0.922	9.527 ± 0.739	6.355 ± 0.640	–

Fig. 7 (c) shows a negative gradient in the [S II]6716, 6731/H α ratio for regions A, B, and C as the aperture size increases, which is the opposite of the aperture effect observed for [O III] 5007/H β. M10 demonstrated that, in low-metallicity H II regions, the [S II]6716, 6731/H α ratio increases as the ionization parameter decreases, a relationship that scales quadratically with the radius of the ionized region. Integrating the entire ionized region into the aperture could thus lead to misinterpretations of the ionization structure, which depends on factors like cluster age and gas distribution. This may align with the trend in the [N II] 6584/Hα ratio shown in Fig. 7(b), although the error bars are quite large. In both cases, region D appears to exhibit the opposite effect, but the error margins are also considerable.

Fig. 7(d) shows no aperture effect for [Ar III] 7135/H α ratio, indicating that the [Ar III] 7135 Å emission line flux follows the same trend as H α: the flux increases with larger apertures while the relative fluxes of these lines remain consistent, regardless of aperture size. However, the associated error bars for this ratio are quite large. Additionally, contributions from older underlying populations would reduce the Balmer line fluxes, thereby modifying the line ratios-intensifying positive gradient effects, such as in Fig. 7 (a), while flattening negative gradients, like those in Figs 7(b) and (c).

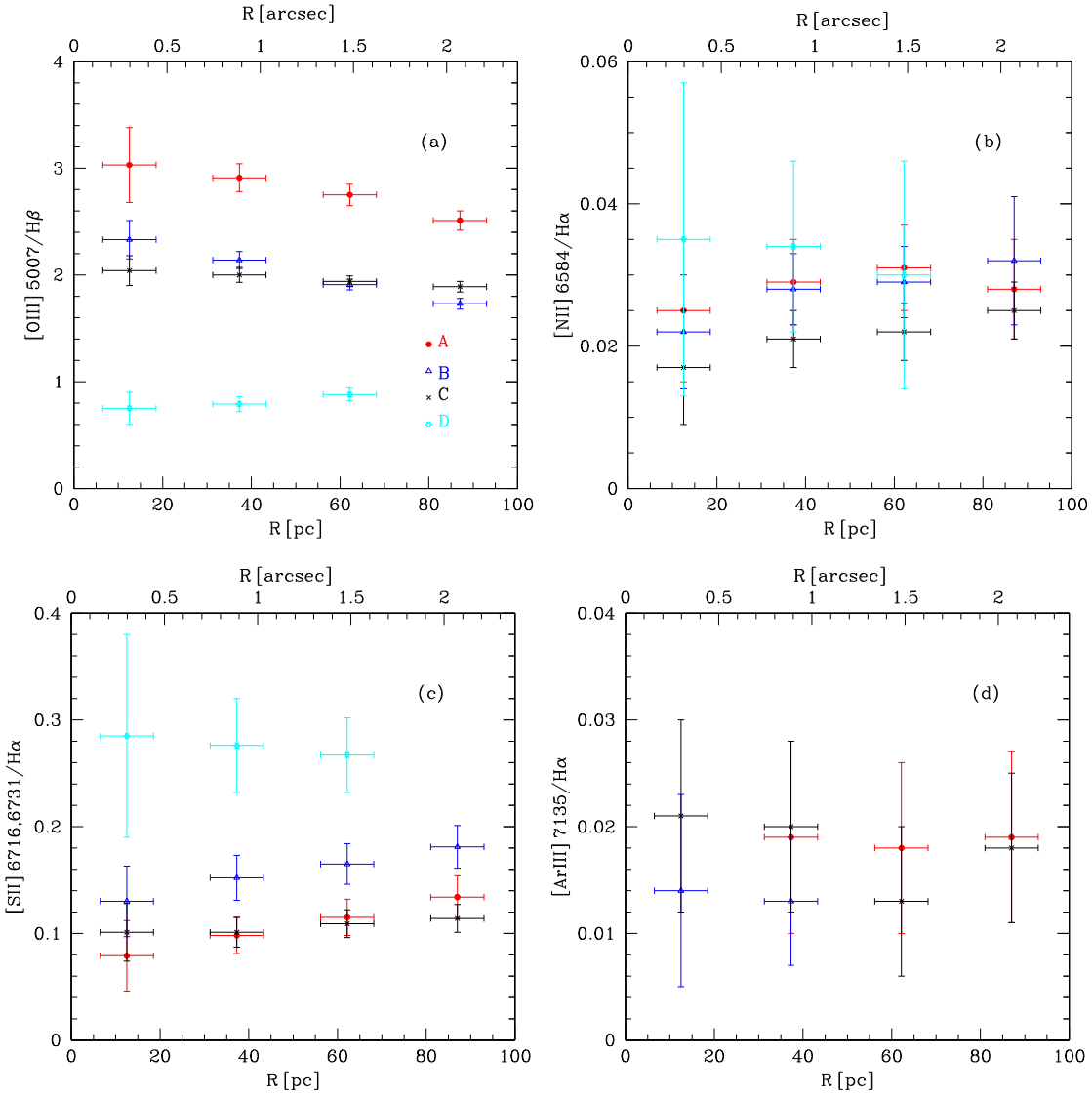

Figure 7. Radial aperture emission line ratios: [O III]5007 / H β (top left), [N II]6584 / H α (top right), [S II]6716, 6731 / H α (bottom left), and [Ar III]7135 / H α (bottom right). Different colours correspond to different H II regions as labelled in the top-left panel. Some aperture effects seen in this figure are discussed in Section 4.2.

Although we have not illustrated this aperture effect for Balmer line equivalent widths, these widths decrease significantly with larger apertures due to greater contributions from intermediate and older underlying populations. This effect is evident in Tables 4 and 5 for H β and H α, respectively, where observations of the whole region would mask the true characteristics of the young ionizing cluster by reducing the Balmer equivalent width values.

4.2.2 The ionization structure

To take full advantage of the fine spatial resolution of the MEGARA IFU, we examined the ionization structure within each of the four regions (A, B, C, and D). For each region, we identified and combined the spaxels with emission across different rings centred around the brightest spaxel in H β (LR-B) and H α (LR-R). We then divided the spectra within each ring by the number of spaxels in that ring to allow for a more direct comparison of the spectra and ionization properties across the different rings.

Table 6 presents measurements of the strongest emission lines observed in the LR-B spectra across consecutive rings. Columns 1 and 2 show the distance from the central brightest spaxel to each ring in arcsec and pc, respectively. Column 3 identifies each ring, The identification of the ring is given in column 3, with 'c' representing the centre of each region and 1, 2, and 3 indicating successive rings outward. Columns 4, 6, 8, and 9 provide the observed fluxes with corresponding errors, in units of $\times 10^{-17}$ erg cm^{-2} s^{-1} for Hγ 4340 Å, Hβ 4861 Å, [O III] 4959 Å, and [O III] 5007 Å, respectively. The equivalent widths (in Å) are shown in columns 5 for H γ and column 7 for H β. Analogously, Table 7 presents the strongest emission lines in the same rings as derived from the LR-R spectra. The first three columns are as in Table 6. Columns 4, 6, 7, 8, and 9 are the observed fluxes, in units of $\times 10^{-17}$ erg cm^{-2} s^{-1} for H α,

Table 6. LR-B emission-line measurements in different rings away from the central brightest spaxel for each of the four ionized regions labelled as A, B, C, and D. Fluxes are given in units of $\times 10^{-17}$ erg s^{-1} cm^{-2} and equivalent widths in Å. Fluxes in this table are not corrected for dust reddening.

(1) d arcsec	(2) d pc	(3) nr	(4) Hγ Flux	(5) Hγ EW	(6) Hβ Flux	(7) Hβ EW	(8) [O III]4959 Flux	(9) [O III]5007 Flux
Region A								
0.3	12.5	c	2.294 ± 0.627	10.23 ± 5.38	5.212 ± 0.524	95.79 ± 64.88	5.260 ± 0.513	15.770 ± 0.912
0.9	37.5	1	1.664 ± 0.219	5.45 ± 1.05	3.553 ± 0.148	29.49 ± 4.50	3.468 ± 0.139	10.260 ± 0.231
1.6	62.5	2	1.151 ± 0.209	7.99 ± 2.49	1.725 ± 0.077	13.95 ± 1.54	1.461 ± 0.086	4.381 ± 0.122
2.2	87.5	3	0.862 ± 0.412	8.88 ± 7.64	0.886 ± 0.055	8.71 ± 1.06	0.524 ± 0.043	1.588 ± 0.064
Region B								
0.3	12.5	c	2.890 ± 0.544	9.26 ± 3.07	5.174 ± 0.339	51.60 ± 16.59	3.843 ± 0.320	12.080 ± 0.487
0.9	37.5	1	1.827 ± 0.264	5.90 ± 1.24	3.706 ± 0.125	33.49 ± 4.42	2.596 ± 0.101	7.763 ± 0.151
1.6	62.5	2	1.171 ± 0.150	3.56 ± 0.56	2.251 ± 0.071	20.17 ± 1.92	1.247 ± 0.062	3.750 ± 0.091
2.2	87.5	3	0.538 ± 0.140	1.92 ± 0.54	1.366 ± 0.059	14.39 ± 1.56	0.573 ± 0.042	1.833 ± 0.069
Region C								
0.3	12.5	c	3.577 ± 0.587	14.52 ± 5.47	6.149 ± 0.346	31.68 ± 6.80	4.159 ± 0.244	12.530 ± 0.451
0.9	37.5	1	2.395 ± 0.371	5.42 ± 1.22	4.760 ± 0.142	21.18 ± 1.95	3.098 ± 0.122	9.459 ± 0.201
1.6	62.5	2	1.874 ± 0.827	12.95 ± 12.36	2.886 ± 0.085	21.10 ± 1.92	1.839 ± 0.073	5.437 ± 0.112
2.2	87.5	3	1.261 ± 0.569	11.51 ± 10.60	1.442 ± 0.061	11.28 ± 1.06	0.859 ± 0.047	2.538 ± 0.077
Region D								
0.3	12.5	c	0.935 ± 0.486	3.61 ± 2.31	1.634 ± 0.231	17.54 ± 6.95	0.522 ± 0.153	1.228 ± 0.166
0.9	37.5	1	0.502 ± 0.206	1.54 ± 0.67	1.422 ± 0.098	14.43 ± 2.51	0.359 ± 0.057	1.135 ± 0.086
1.6	62.5	2	0.512 ± 0.164	1.37 ± 0.46	1.076 ± 0.058	10.32 ± 1.18	0.383 ± 0.053	1.019 ± 0.066

Table 7. LR-R emission-line measurements in different rings away from the central brightest spaxel for each of the four ionized regions labelled as A, B, C, and D. Fluxes are given in units of $\times 10^{-17}$ erg s^{-1} cm^{-2} and equivalent width in Å. Fluxes in this table are not corrected for dust reddening.

(1) d arcsec	(2) d pc	(3) nr	(4) Hα Flux	(5) Hα EW	(6) [N II]6584 Flux	(7) [S II]6716 Flux	(8) [S II]6731 Flux	(9) [Ar III]7135 Flux
Region A								
0.3	12.5	c	11.670 ± 0.504	118.85 ± 31.39	0.293 ± 0.114	0.558 ± 0.141	0.367 ± 0.119	–
0.9	37.5	1	7.930 ± 0.211	87.22 ± 12.12	0.241 ± 0.049	0.431 ± 0.052	0.380 ± 0.049	0.171 ± 0.078
1.6	62.5	2	3.869 ± 0.124	69.40 ± 10.34	0.130 ± 0.035	0.313 ± 0.038	0.221 ± 0.034	0.070 ± 0.039
2.2	87.5	3	2.025 ± 0.080	28.84 ± 3.34	0.039 ± 0.037	0.211 ± 0.035	0.170 ± 0.032	0.041 ± 0.028
Region B								
0.3	12.5	c	11.440 ± 0.609	161.96 ± 61.7	0.250 ± 0.095	0.893 ± 0.137	0.597 ± 0.115	0.163 ± 0.105
0.9	37.5	1	8.752 ± 0.114	127.70 ± 19.86	0.255 ± 0.049	0.818 ± 0.076	0.558 ± 0.065	0.108 ± 0.051
1.6	62.5	2	5.187 ± 0.112	79.46 ± 8.55	0.160 ± 0.033	0.542 ± 0.049	0.378 ± 0.042	–
2.2	87.5	3	3.237 ± 0.091	52.57 ± 5.96	0.128 ± 0.082	0.428 ± 0.040	0.268 ± 0.034	–
Region C								
0.3	12.5	c	13.650 ± 0.454	112.53 ± 22.25	0.238 ± 0.110	0.837 ± 0.132	0.539 ± 0.114	0.292 ± 0.127
0.9	37.5	1	10.340 ± 0.228	89.54 ± 10.43	0.231 ± 0.049	0.590 ± 0.061	0.449 ± 0.056	0.204 ± 0.083
1.6	62.5	2	6.314 ± 0.127	64.09 ± 5.74	0.148 ± 0.033	0.440 ± 0.047	0.297 ± 0.041	0.110 ± 0.045
2.2	87.5	3	3.711 ± 0.085	43.77 ± 3.66	0.120 ± 0.028	0.265 ± 0.030	0.203 ± 0.027	0.062 ± 0.033
Region D								
0.3	12.5	c	4.272 ± 0.348	53.74 ± 17.82	0.150 ± 0.095	0.773 ± 0.144	0.446 ± 0.118	–
0.9	37.5	1	3.400 ± 0.173	36.15 ± 6.09	0.117 ± 0.042	0.552 ± 0.059	0.379 ± 0.051	–
1.6	62.5	2	2.893 ± 0.096	37.92 ± 4.28	0.076 ± 0.071	0.453 ± 0.043	0.303 ± 0.037	–

[N II] 6584 Å, [S II] 6716 Å, [S II] 6731 Å, and [Ar III] 7135 Å. The equivalent width of H α is shown in column 5.

Fig. 8 shows the fluxes (left) and equivalent widths (right) of H α (top), H β (middle), and H γ (bottom) as a function of the distance from the centre of each region. We use different colours to plot the results for each region: A (red), B (blue), C (black), and D (cyan). The decrease in both flux and equivalent width of the Balmer lines with distance reflects the increasing separation from the main ionization source, assumed to be located at the central brightest spaxel.

Fig. 9 displays the radial dependence of some emission line ratios: [O III] 5007 / Hβ (top left), [N II] 6584 / H α (top right), [S II] 6716, 6731 / H α (bottom left), and [Ar III] 7135 / H α (bottom right). We use the same colour code for the regions as in Fig. 8. For regions A, B, and C, we observe a clear ionization structure, with decreasing values of the [O III] 5007 / Hβ ratio and increasing ratios of low-excitation emission lines, such as [S II] 6716, 6731 / H α, and, to a lesser extent, [N II] 6584 / H α. This pattern suggests a decrease in the ionization parameter from the centre to the edge, consistent with a single central ionization source. In contrast, region D shows a slight

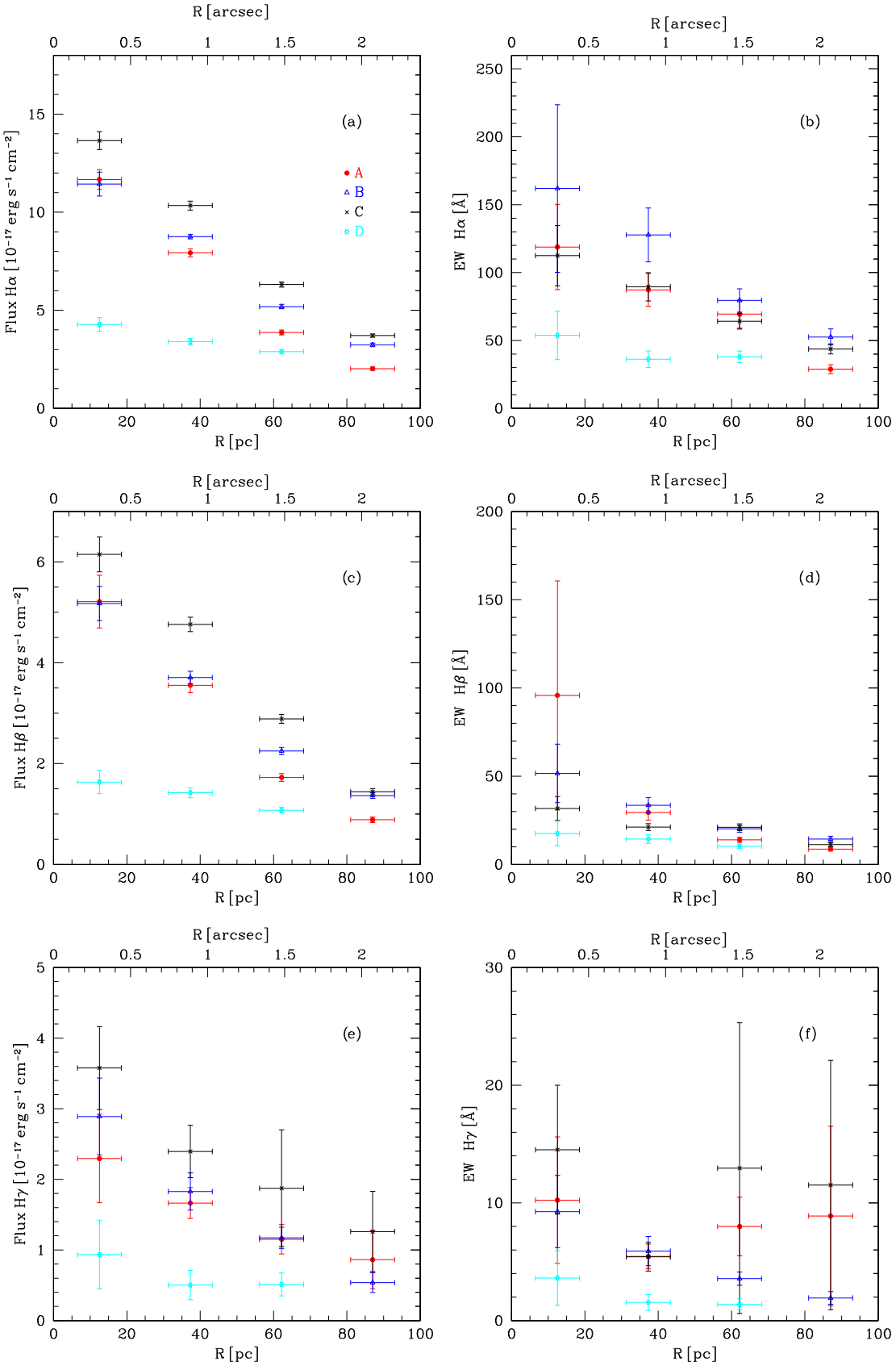

Figure 8. Radial dependence of the observed flux (left) and equivalent width (right) of H α, H β, and H γ.

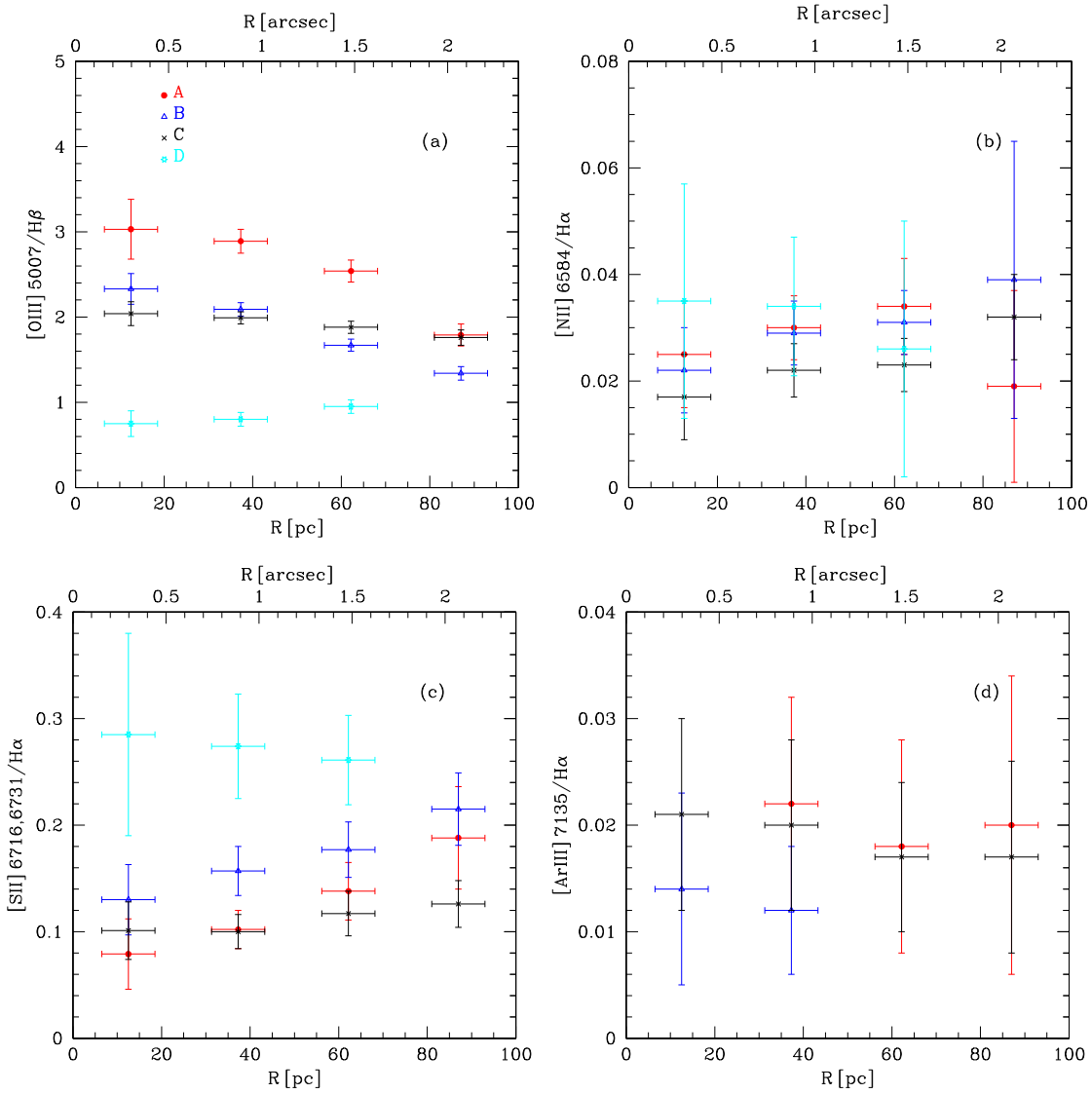

Figure 9. Radial dependence of some emission line ratios: [O III] 5007/Hβ (top left), [N II] 6584/Hα (top right), [S II]Hα (bottom left), and [Ar III] 7135/Hα (bottom right). Different colours correspond to different H II regions as labelled in the top-left panel.

increase in the hardness of the ionization spectrum outward, with a modest rise in the [O III] 5007 / Hβ and a decrease in the [S II] 6716, 6731 / Hα ratio. This suggests that the main ionization source (likely an evolved cluster) may be located approximately 60 pc outward from the centre of region D. The absolute values (prior to normalization) for each ring are listed in Tables 6 and 7.

We have calculated the number of ionizing photons, Q(H), from the observed Hβ flux as

$$Q(\mathrm{H}) = 2.51265 \times F(\mathrm{H}\beta) \times d^2 \times 10^{62}, \quad (2)$$

where Q(H) is the number of ionizing photons in s^{-1}, F(Hβ) is the observed flux of Hβ in units of erg s^{-1} cm^{-2}, and d is the distance to the galaxy in Mpc.

In this case, using the fluxes within the largest aperture for each region, as given in Table 4, and assuming a distance of 8.5 Mpc, the values of log Q(H) are 49.06, 49.16, 49.24, and 48.62 for regions A, B, C, and D, respectively. The radii are 87.5 pc for regions A, B, and C, and 62.5 pc for region D. We will reference these values in the discussion (see Section 5).

At this stage, we aimed to derive the electron-density profiles from the [S II] 6716 Å and [S II] 6731 Å ratio. However, the observed values for this ratio were all above the lower theoretical calibration limit (1.4) (Osterbrock & Ferland 2006; Proxauf, Öttl & Kimeswenger 2014), allowing us to only provide an upper limit of 10 cm^{-3}. Fig. 10 displays a map of this ratio, clearly identifying the four regions. Due to the limited S/N ratio in this spectral range, we could not obtain a more precise determination. We are also unable to determine T_e, as we cannot accurately measure [O III] 4363 Å (see Section 4.2.1).

We estimated the extinction as previously done for the aperture values, but this time using fluxes measured in the different rings. The results are presented in Fig. 11, where we have plotted the observed Balmer ratios Hγ / Hβ for measurements with errors below 0.25 across rings associated with regions A, B, C, and D, as a function of distance from the brightest spaxel, where the ionizing source is assumed to be located.Theoretical values at T_e = 20 000 K and various reddening values, $E(B-V)$, are overlaid in different colours, as labelled, showing consistency with negligible or very low reddening across the regions. Consequently, we calculated the

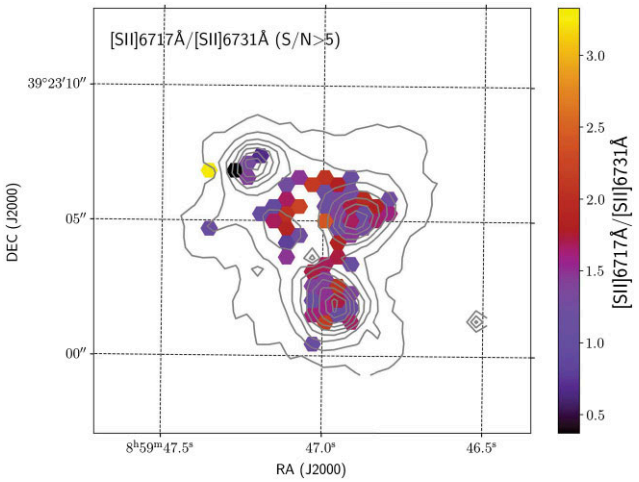

Figure 10. [S II] 6716 Å / [S II] 6731 Å map on MEGARA LCB. We have measured the two lines in 58 spaxels. Values greater than 1.42 exceed theoretical calibrations, indicating that n_e should be lower than 10 cm^{-3}.

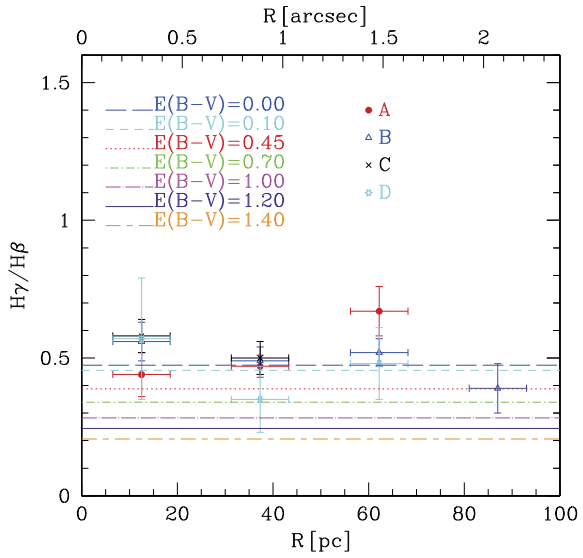

Figure 11. Radial extinction: The observed Balmer ratio Hγ / Hβ, with errors below 0.25, is plotted for the ionization rings of regions A, B, C, and D, as a function of the distance from the brightest spaxel. The theoretical values for T_e = 20000 K and various reddening values, $E(B-V)$, from 0.00 to 1.40, are overlaid in different colours, as labelled in the plot. The results indicate consistency with no or very low reddening across these regions.

number of ionizing photons from Hβ fluxes without applying any dust-extinction correction, as such a low reddening adjustment would have a negligible effect on our conclusions.

We measured the [O III] 4363 Å line flux within the full aperture of region A to estimate T_e and the abundances of O^{++}/H^+ and O^+/H^+, as well as 12 + log(O/H), assuming that the total oxygen abundance is the sum of O^+ and O^{++} abundances. In all cases, we used the expressions provided by Pagel et al. (1992).

Assuming n_e = 10 cm^{-3} and using the fluxes of [O III] 4363, 4959, 5007 Å, and Hβ across the entire aperture of region A, we obtain an electron temperature of T_e = 22 000 ± 6000 K. Given the uncertainty in n_e, we repeated the calculation with n_e = 100 cm^{-3}, and obtained the same result. Comparing this result to the temperature derived using the equation from Pérez-Montero (2014) for n_e = 100 cm^{-3}, yields a consistent value of T_e = 23 500 ± 6000 K, within the margin of error.

Using the value of T_e, we calculate the abundances of O^{++}/H^+ ($1.21 \pm 0.31 \times 10^{-5}$) and O^+/H^+ ($1.37 \pm 0.68 \times 10^{-5}$), yielding an oxygen abundance of 12 + log(O/H) = 7.41 ± 0.15 for region A. This calculation incorporates the flux of [O II] 3726, 3729 Å based on the ratio [O II] 3726, 3729 Å / Hβ from I19, scaled to the actual flux of region A. These results align with the value given by I19 (7.35). However, as a precise abundance determination is not the primary goal of this work, we have requested additional GTC/MEGARA observations of this galaxy with the LR-U grating to obtain a deeper spectrum in the region of the [O III] 4363 Å line.

5 DISCUSSION

5.1 Constraining the properties of the ionizing sources

We used M10 models to constrain the properties of the ionizing clusters. The M10 models, developed with POPSTAR Spectral Energy Distributions, SEDs, and the photoionization code CLOUDY (Ferland et al. 1998), predict the emission line spectrum generated by a single ionizing star cluster based on specific assumptions about gas ionization. These include the number of ionizing photons, Q(H), chemical composition derived from the abundance of different elements; electron density, n_e, ionization bounded geometry, and the characteristics of the young star cluster that determine the hardness of the ionizing spectrum. The POPSTAR spectra depend on various physical properties of the star clusters in the M10 models: mass (ranging from 1.2 $\times 10^4$ to 2.0 $\times 10^5$ $M_\odot$), age (between 1.0 and 5.4 Myr), and overall metallicity (with six values from Z = 0.0001 to Z = 0.05).

We created diagnostic diagrams using the full set of published M10 models (covering all cluster masses and ages) for two metallicities: Z = 0.004 and Z = 0.0004. The metallicity of SDSSJ0859 + 3923 is approximately Z = 0.001, I19, for which there is no corresponding POPSTAR model. We considered two model grids for gas electron density, n_e, 10 and 100 cm^{-3}. The results are shown in Fig. 12: models for Z = 0.0004 and Z = 0.004, are shown as solid and dashed lines in all panels. Models with n_e = 10 cm^{-3} are shown in the left panels (labelled a), while those with n_e = 100 cm^{-3} appear in the right panels (labelled b). Ionizing cluster masses for the M10 models are represented in different colours, as indicated in the top-right of panel b. Each row of two panels shows a specific diagnostic diagram: [S II]6716, 6731 / Hα versus cluster age; [S II]6716, 6731 / Hα versus [O III]4959, 5007 / Hβ; [O III]4959, 5007 / Hβ versus [O II]3727, 3729 / Hβ; [O III]4959, 5007 / Hβ versus [O II]3727, 3729 /[O III]4959, 5007; [O III]4959, 5007 / Hβ versus [N II]6584 / Hα and [O III]4959, 5007 / Hβ versus [N II]6584 / [O II]3727, 3729. Our measurements for the H II regions are plotted as dashed coloured lines (red, blue, cyan, and black for regions A, B, C, and D, respectively) in the first row panels and as filled circles in the same colours in the other diagnostic diagrams. Since we have no direct measurements of [O II] 3727, 3729 Å, we have taken the indirect estimate from I19 for regions B and C (closest to the SDSS DR14 pointing from which the I19 spectrum originates). The I19 value lacks an associated uncertainty, so we cannot include error bars in the diagrams that involve the [O II] 3727, 3729 Å lines.

Based on all diagnostic diagrams,we conclude that regions A, B, C, and D exhibit a metallicity around $Z \simeq 0.004$ or slightly lower, consistent with I19 and our own abundance estimate given in Section 4.2). Our data align with both electron density values, n_e, 10 and 100 cm^{-3}. However, the high [S II] 6716 / [S II] 6731 ratio

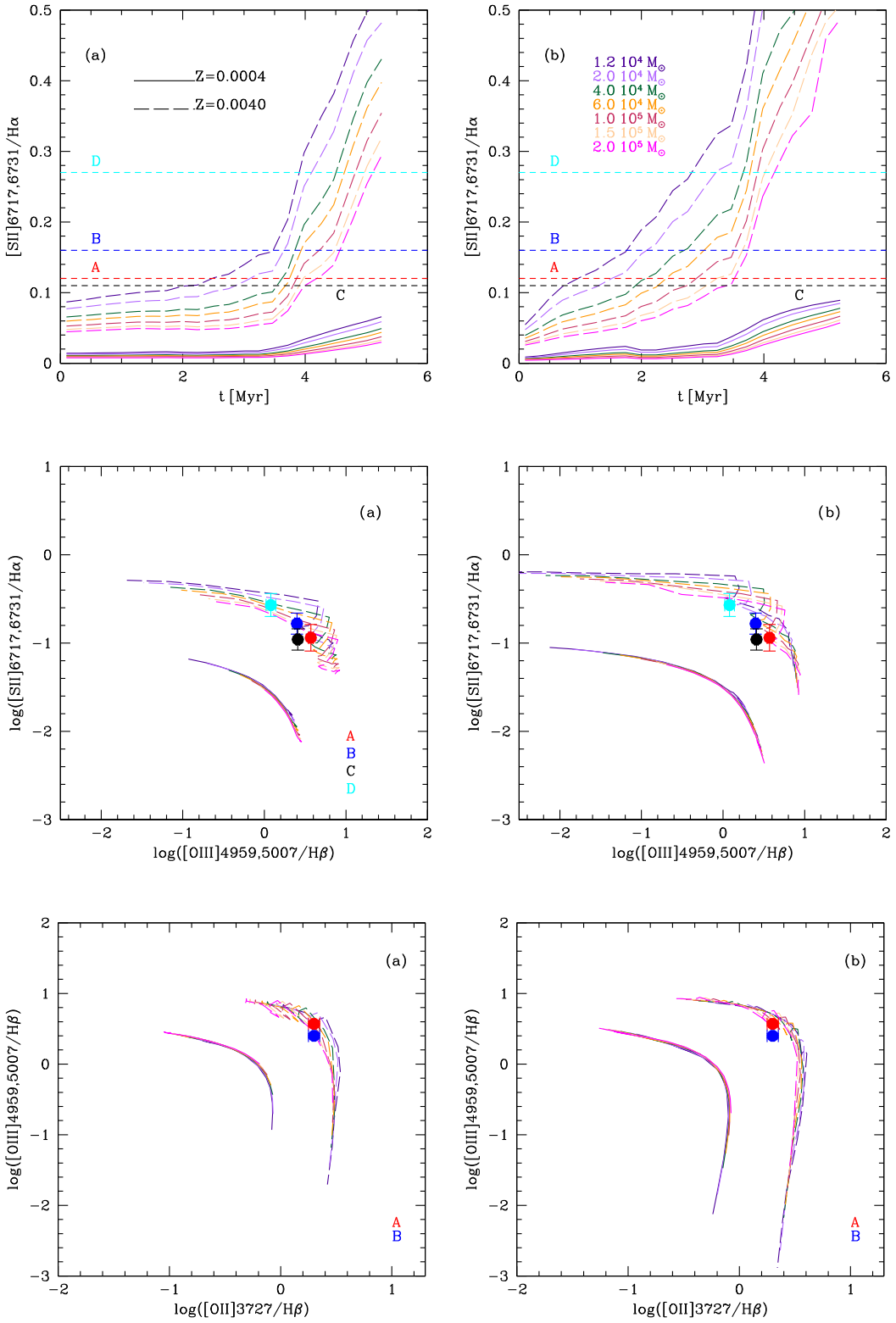

Figure 12. Diagnostic diagrams using POPSTAR M10 models with our results overlaid as large dots. The models include two metallicities: $Z = 0.0004$ (solid line) and $Z = 0.004$ (dashed line), and two electron densities, n_e, 10 cm^{-3} (right panels) and 100 cm^{-3} (left panels). The M10 models represent different star cluster masses, shown in various colours as labelled in the top-right of panel b). Each row in the next two pages of panels shows a different diagnostic diagram: first row, [S II]6716, 6731/Hα versus star cluster age; second row, [S II]6716, 6731/Hα versus [O III]4959, 5007/Hβ; third row, [O III]4959, 5007/Hβ versus [O II]3727/Hβ, fourth row, [O III]4959, 5007/Hβ versus [O II]3727/[O III] 4959,5007; fifth row, [O III]4959, 5007/Hβ versus [N II]6584/Hα, and last row [O III]4959, 5007/Hβ versus [N II]6584/[O II] 3727.

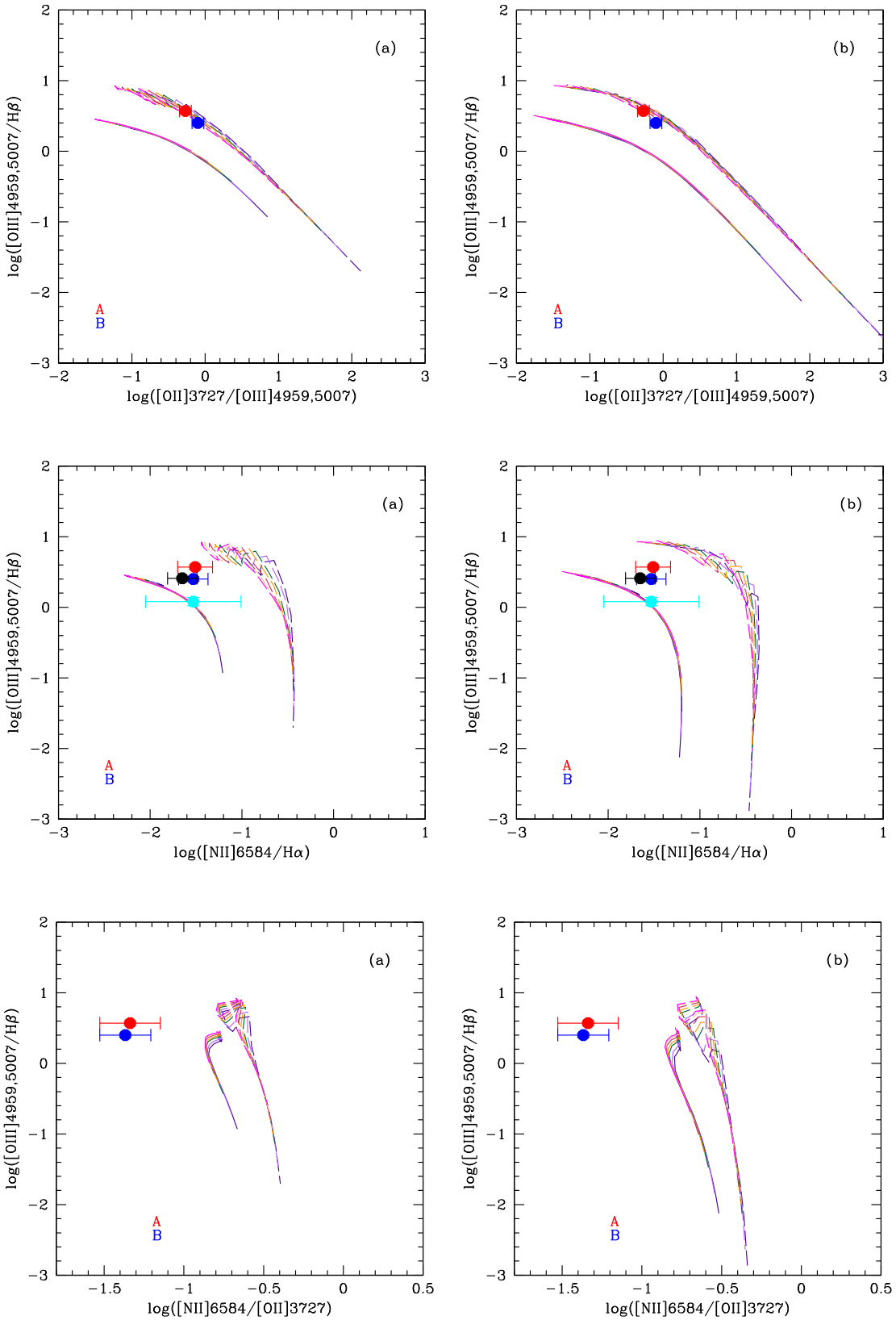

Figure 12. *continued.*

Table 8. Properties of the four H II regions: labelled as A, B, C, and D.

Region	Hβ flux ($\times 10^{-17}$ erg cm^{-2} s^{-1})	Q(H) ($\times 10^{49}$ s^{-1})	log Q(H) (s^{-1})	M_y (M$_\odot$)	Age$_y$ (Myr)	N_{OB} stars	EW Hβ (Å)
A	63.180	1.147	49.060	1379	2.5 ± 1.0 Myr	2	96
B	79.010	1.434	49.157	1724	3.0 ± 1.0 Myr	2	52
C	95.390	1.732	49.238	2081	2.5 ± 1.0 Myr	2	32
D	23.080	0.419	48.622	504	3.5 ± 0.5 Myr	1	18

suggests a very low n_e, so in the discussion we will assume a low electron density of 10 cm^{-3}.

For each region, we calculated the number of ionizing photons from the Hβ flux using equation (2). Assuming all ionizing photons originate from a single cluster, we can estimate limits for the masses of the young clusters responsible for the ionization using POPSTAR models with the IMF from (Kroupa 2002, hereafter K02) and $Z = 0.004$. To do this, we utilized all M10 models between 2.0 and 5.5 Myr (13 ages in M10) and averaged the number of ionizing photons per solar mass for the ionizing cluster, obtaining $\langle \log Q(\mathrm{H}) \rangle = 46.92$ (s^{-1} M$_\odot{}^{-1}$). We then scaled the actual number of ionizing photons in each region, yielding cluster mass estimates of 1.4, 1.7, 2.0, and 0.5 × 10^3 M$_\odot$ for regions A, B, C, and D, respectively. We caution that these low-mass clusters, if they follow a K02 IMF, would only host about two hot stars of late-O or B spectral types in regions A, B, and C, and just one ionizing star in region D. This suggests the IMF may be significantly affected by stochastic effects. Cluster ages can also be estimated from the first row of Fig. (12b), yielding ages of 2.5±1.0 Myr for regions A and C, 3.0 ± 1.0 Myr for region B, and 3.5 ± 0.5 Myr for region D. We acknowledge the uncertainties associated with these estimates due to the low mass of the ionizing clusters and the lack of models for $Z = 0.001$. Additionally, the equivalent widths of the Balmer lines are influenced by underlying stellar populations, which are stronger in regions B, C, and D than in region A, likely explaining the higher Hβ equivalent width observed in region A.

Table 8 summarizes the results for regions A, B, C, and D (as labelled in column 1). Column 2 lists the Hβ flux within the larger aperture in units of $\times 10^{-17}$ erg cm^{-2} s^{-1}. Columns 3 and 4 provide the derived number of ionizing photons, Q(H) (s^{-1}), and its logarithm, log Q(H); columns 5, 6, and 7 contain estimates for the mass of the ionizing cluster, M_y (in M$_\odot$), its age, Age$_y$ (in Myr), and the expected number of hot O-B stars, N_{OB}, all derived from M10 models using a K02 IMF. Finally, column 8 shows the equivalent width of Hβ (in Å) in the central spaxel, representing the stellar populations around the ionizing source.

6 CONCLUSIONS

The MEGARA-IFU observations of SDSSJ0859 + 3923 provide an unprecedented view into this galaxy, with a spatial resolution of 25 pc per spaxel (assuming a distance of 8.5 Mpc) and a high spectral resolving power ($R = 6000$), corresponding to $\sigma = 21$ km s^{-1}. We generated maps of various emission lines and identified five H II regions, labelled A, B, C, D, and E, linking these ionized knots to the UV continuum source visible in the *F336W*/*F438W*/*F606W HST* archive images.

We measured emission-line fluxes within apertures and concentric rings around the brightest spaxel for regions A, B, C, and D, using spatial information to investigate the ionization geometry. We also obtained the total flux across each entire H II region to derive global properties such as dust reddening (in all cases) and nebular properties (for region A only), including electron density, $n_e \leq 100$ cm^{-3}; electron temperature, $T_e = 22\,000 \pm 6000$ K, and oxygen abundance, 12 + log(O/H) = 7.41 ± 0.15 (equivalent to approximately $\frac{1}{22}$ Z$_\odot$.

We uncovered detailed information about these five H II regions that was previously inaccessible with long-slit spectroscopy data, including an analysis of the associated gas kinematics and estimates for the age and mass of the ionizing star clusters based on POPSTAR + CLOUDY models:

(i) Region A: The radius of the detected line-emitting region is approximately 87.5 pc. It exhibits high excitation, no reddening, and low-velocity dispersion (≈10 km s^{-1}). This region has the highest [O III] 5007/Hβ ratio and a faint underlying continuum, consistent with a single unresolved UV-bright source, likely a compact central ionizing cluster. This aligns with the observed radial ionization structure, which shows a decrease in the ionization parameter from centre to edge. We estimate an age of 2.5 ± 1.0 Myr and a mass of ≈1.4 × 10^3 M$_\odot$ for the ionizing cluster.

(ii) Region B: This H II region shares some characteristics with knot, such as a similar radius (87.5 pc), absence of dust reddening, low-velocity dispersion (≈10 km s^{-1}) and a radial ionized structure indicative of a young central ionizing cluster, with an estimated age of 3.0 ± 1.0 Myr and a mass of ≈1.7 × 10^3 M$_\odot$). The underlying blue continuum is stronger than in region A, and several UV-bright regions are present nearby, though none align with the brightest spaxel seen in the emission-line maps. This spatial offset between ionized gas and ionizing stars may result from spatial segregation, especially given the significant stochastic effects in such young, low-mass clusters.

(iii) Region C: It is similar in all respects to region A, with the ionizing cluster estimated to have an age of 2.5 ± 1.0 Myr and a mass of approximately 2.0 × 10^3 M$_\odot$.

The H II regions A, B, and C show high Balmer line equivalent widths at their centres, though these values are lower than those predicted for a single young ionizing cluster, confirming the presence of an older underlying population common to all three regions. The decrease in equivalent width from the centre to the edge of each H II region aligns with their ionization geometry.

(iv) Region D: This is the most compact H II region (radius ≈ 62.5 pc), slightly reddened with $E(B - V) = 0.3 \pm 0.1$ and coincides with a diffuse UV-bright area, possibly an overlap of several individual stars. A slight increase in the hardness of the ionization spectrum is observed moving outward, suggesting that the main ionizing source, with an estimated age of 3.5 ± 1.0 Myr and mass of 0.5 × 10^3 M$_\odot$, is located approximately 60 pc from the centre of the region. The velocity dispersion peaks at 30–40 km s^{-1}, which could be attributed to massive stellar winds (compatible with the cluster's age) or possibly a recent type-II SN explosion. This interpretation is supported by the lower Balmer line equivalent width in the central spaxel of this region, which cannot be explained solely by the young ionizing cluster and the same old underlying population as in the other regions, suggesting the presence of an intermediate-aged population.

(v) Region E: The H II is diffuse, with a faint associated underlying continuum. The line emission is too weak for a detailed diagnostic analysis, and it appears to be associated with only a single unresolved, bright UV continuum source.

The study of these H II regions supports the hypothesis of steady, quiet star formation throughout the galaxy. This is consistent with its low mass and metallicity, as well as the smooth kinematics of the ionized gas, showing no evidence of metal loss through outflows or gas inflow onto the disc.

Finally, we highlight the significance of what we term the *aperture effect*, as discussed in our previous study of the Leoncino galaxy (C22).

In the three highly excited emission-line regions (A, B, and C), the [O III] 5007/Hβ ratio decreases with distance, dropping by up to 40 per cent as aperture size increases compared to values within a small central aperture, with the [O III] 5007 Å flux declining faster than the Hβ flux as aperture expands. If confirmed in other low-metallicity galaxies, this effect would introduce a notable observational bias when searching for XMD galaxies. Currently, candidates are identified in surveys as sources with high [O III] 5007/Hβ ratios, typically measured within a fixed, relatively large slit width or fibre-core size (e.g. SDSS). However, in many of these galaxies, this aperture includes emission from the entire line-emitting region, where the [O III] 5007/Hβ ratio may be significantly lower than near the ionized cluster. This could result in missing a substantial number of low-metallicity candidates. Preliminary results also suggest that the aperture effect becomes more pronounced as metallicity decreases.

ACKNOWLEDGEMENTS

This research has been funded by the project PID2019-107408GB-C41, PID2022-136598NB-C32 and PID2022-136598NB-C33 and by "ERDF A way of making Europe", granted by the Spanish Ministry of Science and Innovation/State Agency of Research MCIN/AEI/10.13039/501100011033, participated by the co-authors MGV, EC, MM, and JI. AGdP, JG, NC, ACM, and SP acknowledge financial support from the Spanish MCIU under the grants RTI2018-096188-B-I00, PID2021-123417OB-I00, and PID2022-138621NB-I00. This work has already being funded with internal R + D projects of FRACTAL S.L.N.E. and INAOE.

This work is based on data obtained with MEGARA instrument, funded by European Regional Development Funds (ERDF), through Programa Operativo Canarias FEDER 2014–2020, and based on observations made with the GTC, installed in the Spanish Observatorio del Roque de los Muchachos of the Instituto de Astrofísica de Canarias, in the island of La Palma.

7 DATA AVAILABILITY

The fluxes of the principal emission lines used in this work are available in the article. The reduced FITS files on which these data are based will be shared on reasonable request to the first author.

REFERENCES

Abazajian K. et al., 2005, AJ, 129, 1755
Abolfathi B. et al., 2018, ApJS, 235, 42
Andrews B-H., Martini P., 2013, ApJ, 765, 140
Aver E., Berg D. A., Hirschauer A. S., Olive K. A., Pogge R. W., Rogers N. S. J., Salzer J. J., Skillman E. D., 2022, MNRAS, 510, 373
Brorby M., Kaarret P., Prestwich A., 2014, MNRAS, 441, 2346
Calzetti D., 1999, Astrophys. Space Sci., 266, 243
Calzetti D., Kinney A. L., Storchi-Bergmann T., 1994, ApJ, 429, 582
Cannon J. M. et al., 2011, ApJ, 739, L22
Cardiel N., Pascual S., 2018, guaix-ucm/megaradrp-calibrations: Release 2018.1
Carrasco E. et al., 2018, Proc. SPIE, 10702, 1070216
Carrasco E. et al., 2022, MNRAS, 509, 6183(C22)
Douna V. M., Pellizza L. J., Mirabel I. F., Pedrosa S. E., 2015, A&A, 559, A44
Ekta B., Chengalur J. N., 2010, MNRAS, 397, 963
Ferland G. J. et al., 1998, PASP, 110, 761
García-Vargas M. L., Bressan A., Díaz A. I., 1995, A&ASS, 112, 13
García-Vargas M. L., Bressan A., Díaz A. I., 1995, A&ASS, 112, 35
García-Vargas M. L., Mollá M., Martín-Manjón M. L., 2013, MNRAS, 432, 2746
Gil de Paz A. et al., 2018, Proc. SPIE, 10702, 1070217
Giovanelli R. et al., 2005, AJ, 130, 2598
Giovanelli R. et al., 2013, AJ, 146, 15
Gómez-Alvarez P. et al., 2018, Proc. SPIE, 10707, 107071L
Guseva N. G., Izotov Y. I., Fricke K. J., Henkel C., 2017, A&A, 599, A65
Haynes M. P. et al., 2011, AJ, 142, 170
Haynes M. P. et al., 2018, ApJ, 861, 49
Hirschauer A. S. et al., 2016, ApJ, 822, 108(H16)
Hirschauer A. S., Salzer J. J., Janowiecki S., Wegner WG. A., 2018, AJ, 155, 82
Howarth I. D., 1983, MNRAS, 203, 301
Izotov Y. I., Thuan T. X., 2007, ApJ, 665, 1115
Izotov Y. I., Thuan T. X., Guseva N., 2012, A&A, 546, A122
Izotov Y. I., Thuan T.X, Guseva N. G., Liss S. E., 2018, MNRAS, 473, 1956
Izotov Y. I., Guseva N. G., Fricke K. J., Henkel C., 2019, A&A, 623, A40(I19)
Kroupa P., 2002, Science, 295, 82(K02)
Kunth D., Östlin G., 2000, A&AR, 10, 1
Martín-Manjón M. L., García-Vargas M. L., Mollá M., Díaz A. I., 2010, MNRAS, 403, 2012(M10)
Mollá M., García-Vargas M. L., Bressan A., 2009, MNRAS, 398, 451(M09)
Osterbrock D. E., 1989, Astrophysics of Gaseous Nebulae and Active Galactic Nuclei. University Science Books, Mill Valley, CA
Osterbrock D. E., Ferland G. J., 2006, Astrophysics of Gaseous Nebulae and Active Galactic Nuclei, 2nd edn. University Science Books, Sausalito, CA
Pagel B. E. J., Edmunds M. G., Blackwell D. E., Chin M. S., Smith G., 1979, MNRAS, 189, 95
Pagel B. E. J., Simonson E. A., Terlevich R. J., Edmunds M. G., 1992, MNRAS, 255, 325
Pascual S., Cardiel N., Picazo-Sánchez P., Castillo-Morales A., Gil de Paz A., 2018, guaix-ucm/megaradrp: v0.8
Pérez-Montero E., 2014, MNRAS, 441, 2663
Prestwich A. H., Tsantaki M., Zezas A., Jackson F., Roberts T. P., Foltz R., Linden T., Kalogera V., 2013, ApJ, 769, 92
Proxauf B., Öttl S., Kimeswenger S., 2014, A&A, 561, A10
Pustilnik S. A., Martin J.M., 2016, A&A, 596, A86
Skilmann E. D., Kennicutt R. C., Hodge P.W, 1989, ApJ, 347, 875
Thuan T. X., Goehring K. M., Hibbard J. E., Izotov Y. I., Hunt L. K., 2016, MNRAS, 463, 4268(T16)
Thuan T. X., Guseva N. G., Izotov Y. I., 2022, MNRAS, 516, L81

This paper has been typeset from a TEX/LATEX file prepared by the author.